The Pennsylvania State University
The Graduate School

FINITE-DIFFERENCE TIME-DOMAIN MODELING OF INFRASOUND PROPAGATION IN A REALISTIC ATMOSPHERE

A Thesis in
Electrical Engineering
by
Sébastien de Larquier

Submitted in Partial Fulfillment
of the Requirements
for the Degree of

Master of Science

August 2010

The thesis of Sébastien de Larquier was reviewed and approved* by the following:

Victor P. Pasko
Professor of Electrical Engineering
Thesis Advisor

Timothy J. Kane
Professor of Electrical Engineering

Kenneth W. Jenkins
Head of the department of Electrical Engineering
Professor of Electrical Engineering

*Signatures are on file in the Graduate School.

Abstract

Atmospheric infrasonic waves are acoustic waves with frequencies ranging from 0.02 to 10 Hz, slightly higher than the acoustic cut-off frequency ($\sim$0.032 Hz), but lower than the audible frequencies (typically 20 Hz-15 kHz). A number of natural events have been identified as generating atmospheric infrasound, such as volcanoes, tornadoes, avalanches, earthquakes, ocean surfaces, lightning, auroral activity, and more recently Transient Luminous Events in the middle atmosphere termed sprites. The importance of infrasound studies has also been emphasized in the past ten years from the Comprehensive Nuclear-Test-Ban Treaty verification perspective. A proper understanding of infrasound propagation in the atmosphere is required for identification and classification of different infrasonic waves and their sources.

In this thesis, one-dimensional (1-D) and two-dimensional (2-D) finite-difference time-domain (FDTD) models of infrasound propagation in a realistic atmosphere have been developed. A computationally efficient parallel version of the two-dimensional model is implemented using a domain decomposition strategy. The models are based on linearized equations of acoustics employing the realistic atmospheric structure and infrasound absorption algorithms advanced by *Sutherland and Bass* [2004]. The absorption is implemented using a recent decomposition technique introduced by *de Groot-Hedlin* [2008].

The FDTD model is used to provide a quantitative interpretation of the recently reported infrasound signatures from pulsating aurora. The pressure perturbations observed on the ground are analyzed as a function of energy flux of precipitating auroral electrons and geometry and altitude localization of the source. The results indicate that fluxes on the order of 50 erg/cm^2/s are needed to explain pressure wave magnitudes of 0.05 Pa observed on the ground. This energy is unlikely to be provided exclusively by precipitating electrons, and Joule heating associated with the electrojet modulated by the pulsating aurora may be responsible for part of

the deposited energy.

Following recent experimental results on infrasound from Transient Luminous Events (TLEs) in the upper atmosphere termed sprites, the FDTD model is used to provide qualitative explanations of close range ground observations: results suggest that the vertical extent of the sprites combined with the altitude dependency of the transverse extent of filamentary structures in sprites are responsible for the inverted chirp signal observed on the ground. Using HARPA ray-tracing simulations, a mechanism explaining long range observations is proposed based on initial suggestions by *Farges et al.* [2005]. Efforts to provide FDTD results on long range observations are in progress.

Table of Contents

List of Figures

List of Symbols

Δr, Δz	Discretization steps in cylindrical coordinates r, z (m)
c_s	Sound speed (m/s)
$\rho = \rho_0 + \tilde{\rho}$	Total neutral density background + perturbation (kg/m^3)
$p = p_0 + \tilde{p}$	Total pressure background + perturbation (Pa)
μ	Coefficient of viscosity (kg/m/s)
ν	Kinematic viscosity (m^2/s)
ξ	Absorption coefficient (s^{-1})
α	Atmospheric absorption coefficient of sound (dB/km)
g	Gravitational acceleration (m/s^2)
H	Scale height (m)
ω_0	Acoustic cut-off frequency (rad/s)
N	Brunt-Väisälä frequency (rad/s)
$\vec{v} = v_r\hat{r} + v_z\hat{z}$	Velocity vector (m/s)
$\vec{v}^{\alpha} = v_r^{\alpha}\hat{r} + v_z^{\alpha}\hat{z}$	Velocity vector in the NPML region (m/s)
$\tilde{p}^{\alpha}, \tilde{r}^{\alpha}$	Pressure and density perturbations in the NPML region
$\gamma' = 1.4$	Ratio of specific heats (c_p/c_v)
ρ_s, p_s	Density and pressure at a reference height ($z = 0$)
$\frac{\tilde{p}}{p_0(z)}\sqrt{\frac{p_0(z)}{p_0(z_{\text{ref}})}}$	Normalized pressure perturbation, where z_{ref} is arbitrary

Acknowledgments

I am very grateful to my advisor, Dr. Victor Pasko, for offering me the opportunity to investigate a very exciting field of study. His guidance and support not only led me to the scientific results presented in this thesis, but also to discover and appreciate the world of research.

I would like to thank Dr. Timothy Kane for always being there to answer my many questions and for providing me with invaluable advice and support.

I would like to thank Drs. Hans Stenbaek-Nielsen, John V. Olson and Charles R. Wilson of the University of Alaska, Fairbanks for their insightful directions and considerable help as co-authors of my first paper.

I would also like to thank Drs. Douglas Drob, Elisabeth Blanc, Thomas Farges and Catherine de Groot-Hedlin for discussions at the CEDAR and AGU meetings.

I am also indebted to the CEDAR community for the many helpful discussions and lectures during the 2009 Summer Workshop.

Finally, I would like to especially thank my family for understanding that I do not love infrasound more than I love them in spite the numerous times I had to ignore their emails and requests for some news because my model was not working.

Sébastien de Larquier,
University Park, PA
March 29, 2010

This research was supported by the National Science Foundation under grant AGS-0836391 to the Pennsylvania State University.

Chapter 1

Introduction

1.1 Review of Past Work

In order to better grasp the context and motivations of the problems detailed in this thesis, it is important to first review past scientific results. Infrasound importance in the geosciences can be partially demonstrated by a fast growth of related publications in refereed scientific literature. A search on the Web of Science [http://apps.isiknowledge.com/] indicates that the number of publication on propagation of infrasonic wave in the Earth atmosphere has increased by a factor of ten in the past 10 years (see Figure 1.1). As a result, the literature provides insight into a limited but growing number of phenomena, most of them are still poorly understood. This thesis primarily focuses on infrasonic events generated by middle to upper atmospheric sources.

1.1.1 Observation of Infrasound

Atmospheric infrasonic waves are acoustic waves with frequencies ranging from 0.02 to 10 Hz [e.g., *Blanc et al.*, 1985] (see Figure 1.2). The attenuation of acoustic waves in the atmosphere is approximately proportional to the frequency squared, so unlike audible frequencies, infrasound can propagate thousands of kilometers through the tropospheric, stratospheric, mesospheric and lower thermospheric regions, exhibiting global propagation characteristics [*Drob and Picone*, 2003]. It can be noted with reference to Figure 1.3(a) that under typical conditions in the lower

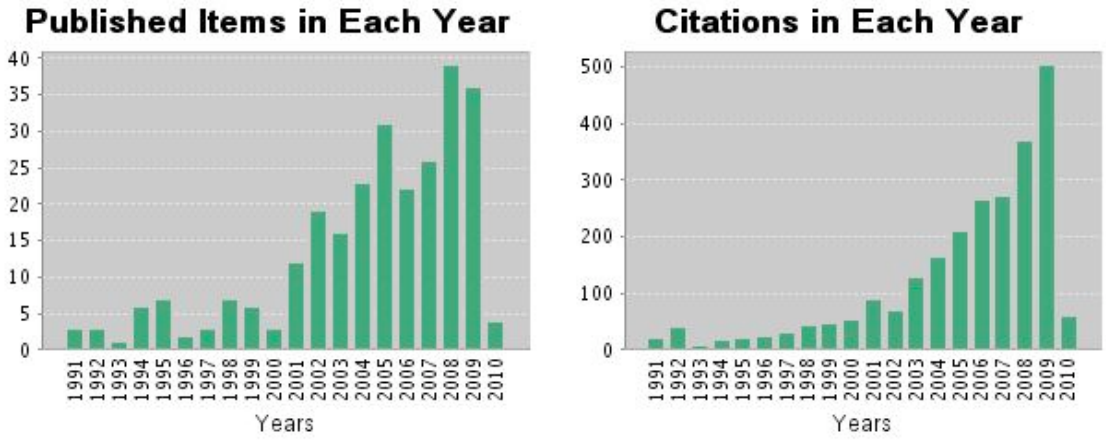

Figure 1.1. Citation report on publications in refereed scientific literature with the keywords "infrasound" and "geosciences" [http://apps.isiknowledge.com/].

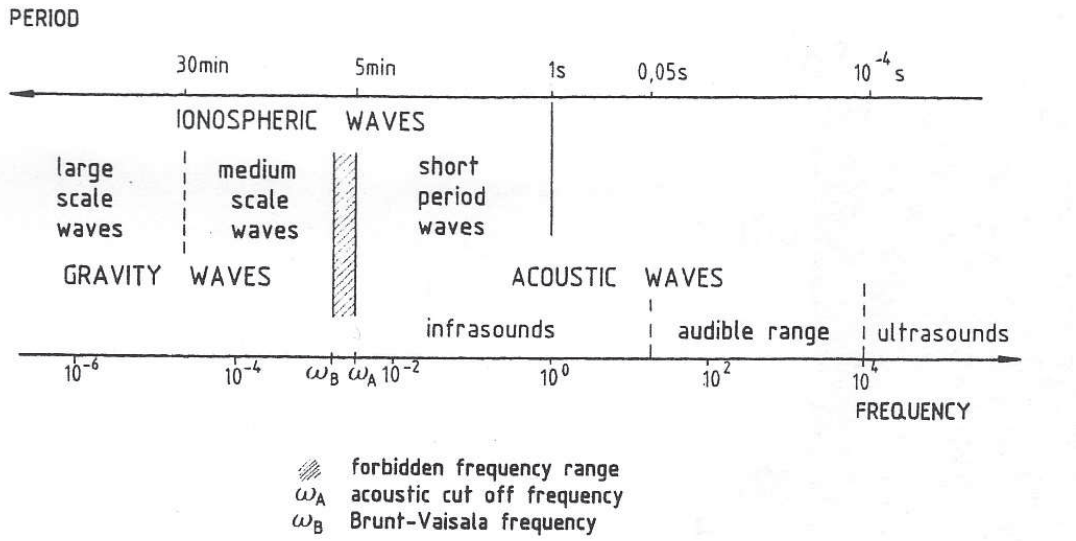

Figure 1.2. Classification of atmospheric waves [*Blanc*, 1985]. The infrasonic waves have frequencies higher than the acoustic cut-off frequency but lower than the audible frequency range 20-1.5×10^4Hz.

atmosphere the absorption of 1 Hz infrasonic waves can be neglected. It is nominally less than 0.01 dB/km so even for path lengths on the order of of one-tenth the radius of the Earth absorption would be less than 10 dB [e.g., *Sutherland and Bass,* 2004]. At the same time the absorption of the same 1 Hz wave at 160 km is more than 10 dB/km (Figure 1.3a). The Earth's thermosphere lies above about 80 km so for infrasonic waves launched upward from lower altitudes, this is the last

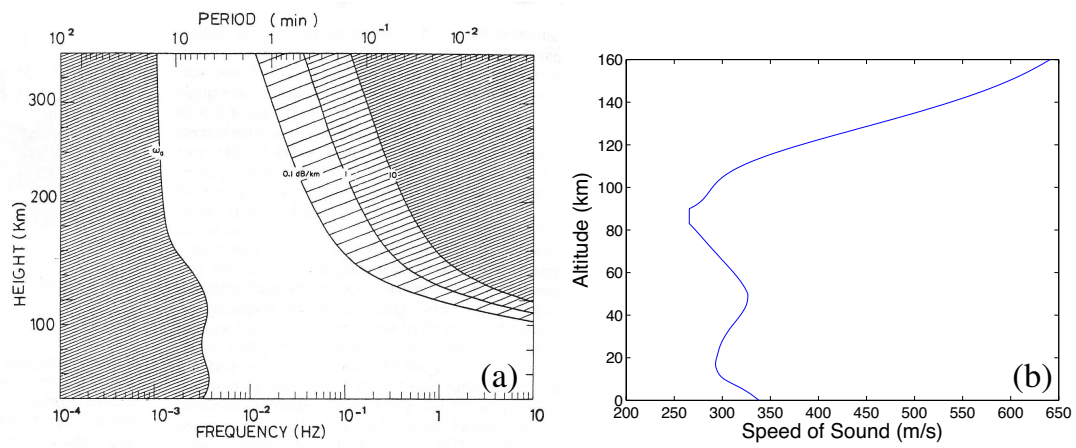

Figure 1.3. Filter effect of the atmosphere considering the limitations imposed by absorption and acoustic cut-off [*Georges*, 1968; *Blanc*, 1985]. (b) Atmospheric speed of sound model from [*Sutherland and Bass*, 2004].

refractive layer to turn the waves back toward the Earth, and with an absorption of 10 dB/km, waves at a frequency of 1 Hz would not make it to the thermosphere and then back down to Earth [*Sutherland and Bass,* 2004]. In addition to their attenuation properties the propagation of infrasonic wave packets is significantly controlled by their refraction, reflection and ducting due to the speed of sound variation as a function of altitude in the Earth's atmosphere (Figure 1.3b), and by the altitude dependent pattern of winds (i.e., zonal and meridional) [e.g., *Drob et al.,* 2003].

A number of natural events have been identified as generating atmospheric infrasound. Powerful explosions were known to generate pressure waves since the explosion of the Krakatoa volcano in 1883 or the Great Siberian Meteorite in 1909. Both events were recorded around the world by very sensitive barometers [*Bedard and Georges*, 2000].

Volcano generated infrasound has also been reported, and is not exclusively from the blasts associated with active volcano erruptions. Pre-eruptions signals called Long Period (LP) seismic events have been recorded around Mount St Helens [*Matoza et al.*, 2006]. These events are the result of magma pressure change in the volcano's magma channels. Measuring the intensity and frequency of LP events can help retrieve information on an upcoming eruption. Seismic generated infrasound also helps study earthquakes.

Lightning has been suggested as generating infrasound, by C.T.R. Wilson in 1920 [*Wilson*, 1920]. A study using infrasound arrays and an electromagnetic (EM) lightning detection network called SAFIR (Surveillance et Alerte Foudre par Interférometrie Radioélectrique) has been conducted in 2006 by *Assink et al.* [2008]. The results of this study show a high correlation between detections of infrasonic and electromagnetic signals from lightning up to distances of 50 km. Recently, *Pasko* [2009] provided an extensive review of literature on infrasound radiated from thunderstorms and lightning.

Transient Luminous Events (TLEs) termed sprites have recently been identified as generating infrasound [e.g., *Farges et al.*, 2005; *Farges and Blanc*, 2010; *Liszka and Hobara*, 2006]. Sprite-attributed infrasonic signals are observed from 50 km to more than 400 km horizontal distances from the source. Close observations reveal an inverted chirp signal with high frequency infrasonic waves leading low frequency components, while long range observations show chirp signatures (i.e., with leading low frequencies), both exhibiting long time scales ($\sim$1-2 min) relatively to sprites time scales ($\leq$100 ms). These specific signatures have yet to be explained.

Another example of infrasound sources is associated with aurora activity. Video data from pulsating auroras above Fairbanks, Alaska, have been recently correlated with infrasound observations [*Wilson et al.*, 2005]. Infrasonic data for a specific pulsating aurora has been collected at the infrasound array I53US and provides very sensitive and accurate measurement of pressure perturbation amplitude and incident angle. Additionally, infrasonic waves from supersonic auroral arcs have also been observed [*Wilson and Nichparenko,* 1967; *Wilson,* 1967].

These are but a limited sample of the many possible natural sources of atmospheric infrasound. The most important artificial sources studied for the past ten years are explosions, with the intent of monitoring possible nuclear explosions. In the frame of the Comprehensive Nuclear-Test-Ban Treaty (CTBT), 60 infrasound arrays have been deployed all over the world to monitor infrasound activity in the atmosphere [*Le Pichon et al.*, 2008]. A nuclear explosion would be observed thousands of kilometers away form its point of origin, thus being recorded by more than one station, which allow to detect the exact location of the explosion. Fortunately nuclear explosions are not a daily event and the CTBT infrasonic arrays provide invaluable resources for scientists to continuously observe natural sources

of infrasonic waves.

The availability of global infrasound data, combined with a significant improvement in recent years of infrasound detectors has lead scientist to consider infrasound as a potential remote sensing tool. In fact, sound waves heard across the English Channel in 1901 were used by *Whipple* [1926] to postulate the existence of the tropopause and the stratospheric temperature inversion. Interestingly, optical, electromagnetic and in-situ measurements of the atmosphere are still called "soundings" today [*Drob et al.*, 2009].

This MS thesis represents a focused modeling effort which will attack a limited set of unsolved problems related to infrasonic wave production by sprites and pulsating auroras.

1.1.2 Modeling of Infrasound

To achieve a full interpretation of measured infrasonic signals, one needs a proper understanding of infrasound propagation through the atmosphere.

Gossard and Hooke [1975] summarized the theory of the general case of nonlinear wave propagation in the atmosphere, which included infrasonic waves among others. This model can be easily applied to the more specific case of a linearly propagating acoustic wave.

In a realistic atmosphere, there exist temperature variations with height that can severely alter the propagation of infrasound. As a result, the waves experience refraction and even reflection. Rather than assuming an isothermal system with a purely exponential density profile, it is possible to describe atmospheric regions as discrete layers of varying temperature or density. *Gossard and Hooke* [1975] reviewed several classical solutions for layered systems.

Numerical simulation of infrasound is a very helpful tool. The main approach of infrasound simulation is classical ray tracing [*Drob et al.* 2003]. Ray tracing formulations provide a way to calculate infrasound propagation paths, including reflection heights, travel times, and wave front arrival angles. This, however, is usually limited to simple monochromatic sources, which do not accurately represent realistic natural or artificial sources. Another method based on parabolic equations [e.g., *Lingevitch et al.,* 2002] is also used for infrasound propagation

analysis. The ray tracing and parabolic equation solutions provide correct predictions for infrasound propagation for relatively short distances of 300-400 km [e.g., *Arrowsmith et al.,* 2007]. The current ability to model and interpret observations for long range (>1000 km) infrasonic propagation is limited [*Arrowsmith et al.,* 2007].

An alternative to ray tracing is a direct solution of acoustics equations using finite-difference time-domain (FDTD) approach. Recently, *Pasko* [2009] used a fourth order in space and second order in time FDTD scheme to study the radiation of infrasound associated with lightning discharges. FDTD modeling is widely used by the electromagnetics community as it represents one of the simplest and flexible means for finding electromagnetic solutions in a medium with arbitrary inhomogeneities [e.g., *Taflove and Hagness,* 2000]. In addition opposed to other numerical methods, the spatial discretization of FDTD is a direct translation of real world objects, which makes it easy to model complex environments such as buildings or entire cities. FDTD schemes provide a very straightforward way of discretizing partial differential equations. While atmospheric infrasound studies do not necessarily need to model buildings or complex structures, they could directly benefit from the possibility of modeling sources with complex geometries. It should be noticed that use of FDTD methods for atmospheric infrasound modeling is fairly recent [*de Groot-Hedlin*, 2008], due to intrinsic intensive computational needs of FDTD schemes. At present, there is only one paper known to us by a French group of authors [*Millet et al.,* 2007], which utilizes similar techniques for long-range propagation of infrasonic waves in realistic atmosphere. The research in this MS Thesis extends this type of techniques to solutions of specific infrasound propagation problems related to sprites and auroras.

1.2 Problem Formulation

The previous section shows the importance and range of applications of infrasound studies. A proper understanding of infrasound propagation in the atmosphere is required for identification and classification of different acoustic waves and their sources. The variety of sources suggest that developing a model of infrasound generation and propagation for a single source would limit the range of applications

of our understanding of infrasonic waves. However, if a model is developed that accurately describes the behavior of infrasound in a realistic atmosphere for any perturbation, a variety of sources can be used as inputs to the model and model calculations can be used to perform inverse calculations from experimental data.

Atmospheric conditions play a very important part in infrasound propagation. Many different models exist to describe atmospheric quantities such as temperature, pressure and density. In subsequent section, we will give a description of the model used in our computation as well as the specific model modifications required by our approach. Acoustic absorption depends not only on altitude, but also on the wave frequency and we will use the most up-to-date techniques to accurately describe and model related effects.

The purpose of this work is to develop a finite-difference time-domain numerical model that will efficiently predict infrasound propagation in a realistic atmosphere for a wide range of sources with different geometries and spectral content. This model can then be used to understand specific infrasound signatures observed in experiments.

Following a publication by *Wilson et al.* [2005], where pulsating auroras have been reported as a possible infrasound source, we will give a detailed analysis of infrasound generated by a modeled pulsating aurora.

An investigation of infrasonic signals from sprites based on recent observations by *Farges et al.* [2005] and *Farges and Blanc* [2010], will be the second application of the FDTD model presented in this thesis.

1.3 Organization of the Thesis

Chapter 1 has begun our discussion with a review of the relevant literature on the observation and theory of infrasound propagation. Chapter 2 will proceed with a detailed study of the mathematical description of infrasound propagation through a compressible heterogeneous atmosphere. We will also consider the compressible linear case as an analytical tool to study infrasonic wave propagation. Analytical solutions are helpful in understanding the phenomena without needless complications or additional numerical methods. A description of the atmospheric models used as the simulations background, with a particular emphasis on acoustic ab-

sorption will be presented in this chapter. Chapter 3 will discuss the numerical model and its implementation. Chapter 4 will illustrate an application of infrasound modeling to understand observations of infrasonic radiation from pulsating auroras. Chapter 5 will extend infrasound analysis to recent observations of infrasonic signals correlated with sprites. Chapter 6 will outline conclusions and propose future developments relevant to the present work.

1.4 Scientific Contributions

This thesis makes several contributions to the field of atmospheric physics that can be summarized as follows:

- Development of 1-D and 2-D finite-difference time-domain (FDTD) models based on linearized equations of acoustics employing the realistic atmospheric structure and infrasound absorption algorithms advanced by *Sutherland and Bass* [2004].

- Implementation, in framework of the 1-D and 2-D FDTD models, of a decomposition technique for efficient modeling of infrasound absorption in a realistic atmosphere recently proposed by *de Groot-Hedlin* [2008].

- Parallelization of the 2-D model using a domain decomposition technique enabling faster computation and memory distribution.

- Our studies of infrasound produced by pulsating auroras confirm the validity of assumption of *Wilson et al.* [2005] concerning 1-D (planar) representation of the source of pulsating aurora. However, results also demonstrate critical importance of scaling of pressure perturbation proportionally to root square of ambient pressure in a gravitationally stratified atmosphere for derivation of accurate magnitudes of infrasonic waveforms on the ground.

- Modeling results on infrasound from pulsating auroras indicate that fluxes on the order of 50 erg/cm^2/s are needed to explain pressure waves magnitudes of 0.05 Pa observed on the ground. This energy is unlikely to be provided exclusively by precipitating electrons, and Joule heating associated with the

electrojet modulated by the pulsating aurora may be responsible for part of the deposited energy.

- Modeling results of sprite generated infrasound observed at close range (∼75 km) emphasize the importance of both the atmospheric absorption and scaling of transverse dimension of filamentary structures (streamers) in sprites as a function of altitude to explain the observed inverted chirps.

- Modeling results confirm the validity of an assumption by *Farges et al.* [2005] that the infrasound signature from sprite observed at long distance from the source is due to a ground-thermosphere-ground propagation of the infrasound radiated from the sprite.

- Preliminary results from ray-tracing analysis suggest that sprite generated infrasound observed at long distance from the source (∼400 km) are generated by a deposition of energy within a small vertical extent at a given altitude (∼70-80 km) within the horizontal extent of the sprite.

Most of the results presented in this thesis have been published in Geophysical Research Letters [*de Larquier et al.*, 2010], and presented at 2009 CEDAR workshop [*de Larquier and Pasko*, 2009a] and 2009 AGU Fall meeting [*de Larquier et al.*, 2009b].

Chapter 2

Model Formulation

2.1 Euler Equations

To describe infrasound propagation in the atmosphere we use Euler's equations. They express the conservation of density ρ, momentum $\rho\vec{v}$ and energy E in an inviscid ideal gas. Their generalized form can be written as follows [*Hines*, 1960; *Potter*, 1973, ch. 9]:

$$\frac{\partial \rho}{\partial t} + \vec{\nabla} \cdot \rho\vec{v} = 0 \tag{2.1}$$

$$\frac{\partial \rho\vec{v}}{\partial t} + \vec{\nabla} \cdot (\rho\vec{v}\vec{v}) = -\vec{\nabla}p - \rho\vec{g} \tag{2.2}$$

$$\frac{\partial E}{\partial t} + \vec{\nabla} \cdot ((E+p)\,\vec{v}) = -\rho v_z g \tag{2.3}$$

where the energy equation and the equation of state for an ideal gas are defined as [*Potter*, 1973, ch. 9]:

$$E = \rho\epsilon + \frac{1}{2}\rho\,(\vec{v}\vec{v}) \tag{2.4}$$

$$\epsilon = \frac{p}{(\gamma' - 1)\,\rho} \tag{2.5}$$

Euler's equations as expressed in (2.1), (2.2) and (2.3) do not include any losses, like viscosity, thermal diffusion, or molecular relaxation. Those losses play

an important role at high altitude on infrasound propagation [e.g., *Evans*, 1972; *Sutherland and Bass*, 2004]. To simplify the mathematical analysis of Euler's equations we will initially ignore absorption terms, and will introduce them in the next chapter.

Gravitational stratification of the atmosphere is included in the momentum (2.2) and energy (2.3) equations through the terms containing the gravitational acceleration g. Having defined the speed of sound $c_s^2 = \gamma p/\rho$, we can find equilibrium solutions of equation (2.2):

$$\begin{pmatrix} \rho_0 \\ p_0 \end{pmatrix} = \begin{pmatrix} \rho_s \\ p_s \end{pmatrix} \exp\left(- \int_{z_s}^{z} H^{-1} dz' \right) \tag{2.6}$$

where $H = RT/Mg = c_s^2/\gamma g$ is the scale height. It is integrated from a reference height z_s to a height of interest z. This result shows that density and pressure decay exponentially with altitude.

2.2 Linear Dispersion Relation

To further understand the behavior of waves motion described by Euler's equations we need to derive a dispersion relation. For that purpose we write Euler's equations in a two-dimensional linearized form:

$$\frac{\partial \tilde{\rho}}{\partial t} = -\rho_0 \frac{\partial \tilde{v}_x}{\partial x} - \rho_0 \frac{\partial \tilde{v}_z}{\partial z} - \tilde{v}_z \frac{\partial \rho_0}{\partial z} \tag{2.7}$$

$$\frac{\partial \tilde{v}_x}{\partial t} = -\frac{1}{\rho_0} \frac{\partial \tilde{p}}{\partial x} \tag{2.8}$$

$$\frac{\partial \tilde{v}_z}{\partial t} = -\frac{1}{\rho_0} \frac{\partial \tilde{p}}{\partial z} - \frac{\tilde{\rho} g}{\rho_0} \tag{2.9}$$

$$\frac{\partial \tilde{p}}{\partial t} = -v_z \frac{\partial p_0}{\partial z} - \gamma p_0 \left(\frac{\partial \tilde{v}_x}{\partial x} + \frac{\partial \tilde{v}_z}{\partial z} \right) \tag{2.10}$$

where $\tilde{v}_x$ and $\tilde{v}_z$ are the wave perturbation velocities and $\tilde{p}$ and $\tilde{\rho}$ are perturbations pressure and density, respectively.

Assuming plane wave solutions proportional to $\exp\left(j\left(\omega t - k_x x - k_z z\right)\right)$ and an isothermal system, we can combine equations (2.7), (2.8), (2.9) and (2.10) and

obtain:

$$\frac{\partial^2 \tilde{v}_z}{\partial z^2} + \frac{1}{\rho_0}\frac{\partial \rho_0}{\partial z}\frac{\partial \tilde{v}_z}{\partial z} + \left[\frac{\omega^2 - \omega_0^2}{c_s^2} - \frac{\omega^2 - N^2}{v_{px}^2}\right]\tilde{v}_z = 0 \tag{2.11}$$

where $v_{px} = \omega/k_x$ is the horizontal phase velocity.

To obtain a more explicit equation, we need to account for the gravitational stratification of the atmosphere. As a wave propagates upward in the atmosphere it will experience a decrease of neutral density. To respect kinetic energy conservation, the perturbation velocity will have to decrease accordingly. We find that this increase is proportional to $(\rho_0/\rho_s)^{-1/2}$. We introduce a normalized vertical velocity perturbation $\tilde{w}_z = (\rho_0/\rho_s)^{1/2}\,\tilde{v}_z$ and from (2.11) obtain:

$$\frac{\partial^2 \tilde{w}_z}{\partial z^2} + \left[\frac{\omega^2 - \omega_0^2}{c_s^2} - \frac{\omega^2 - N^2}{v_{px}^2}\right]\tilde{w}_z = 0 \tag{2.12}$$

This is a wave equation governed by the following linear dispersion relation:

$$k_z^2 = \frac{\omega^2 - \omega_0^2}{c_s^2} - \frac{\omega^2 - N^2}{v_{px}^2} \tag{2.13}$$

where $\omega_0 = g\gamma/2c_s$ is the acoustic cut-off frequency and $N = \frac{g}{c_s}\sqrt{\gamma - 1}$ is the Brunt-Väisälä resonance frequency for the isothermal, compressible case. From this simplified derivation, we can draw the propagation diagnostic diagram [*Gossard and Hooke*, 1975] shown in Figure 2.1.

For audible acoustic waves, we would work on the upper right part of the acoustic domain, thus having a well known dispersion relation $k_x^2 + k_z^2 = \omega^2/c_s^2$. For infrasound however, we work with frequencies close enough to the acoustic cut-off frequency so that the dispersion relation is $k_x^2 + k_z^2 = \left(\omega^2 - \omega_0^2\right)/c_s^2$. Among other consequences, this dispersion relation will result in noticeable differences between phase and group velocities at low frequencies.

2.3 Standard Atmospheric Profiles

To properly implement the mathematical model, we need an accurate description of the atmosphere. Different models are available for that purpose, with different

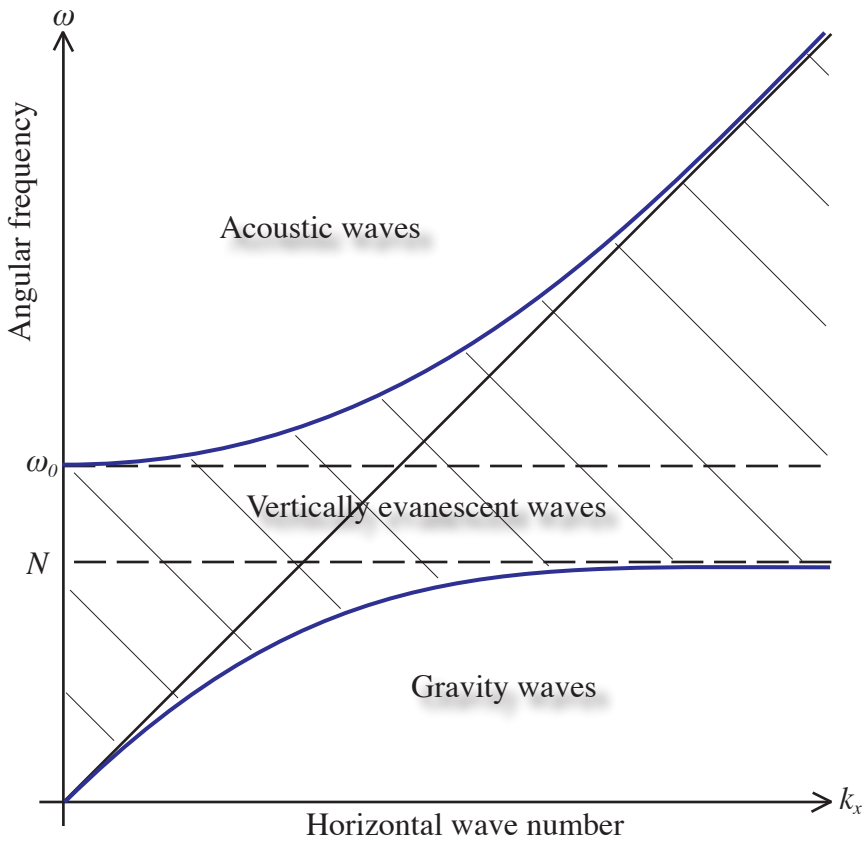

Figure 2.1. Frequency versus horizontal wavenumber plot, schematically illustrating domains of different wave types.

level of complexity. At its current stage of development, our model does not account for winds or geographically specific weather conditions. A more general approach is adopted with a standardized atmosphere described by *Sutherland and Bass* [2004]. This model provides temperature, pressure, molecular fractions and sound absorption profiles. The following section gives an overview of absorption profiles. The temperature, pressure, and speed of sound profiles are illustrated in Figure 2.2. This representation of the atmosphere, even if idealized (it is a global model intended to represent atmospheric conditions anywhere on the planet), still gives an accurate description of its important characteristics:

- Pressure and density scaling: neutral pressure and density decrease exponentially with altitude, in agreement the hypothesis used in the mathematical description (Section 2.1).

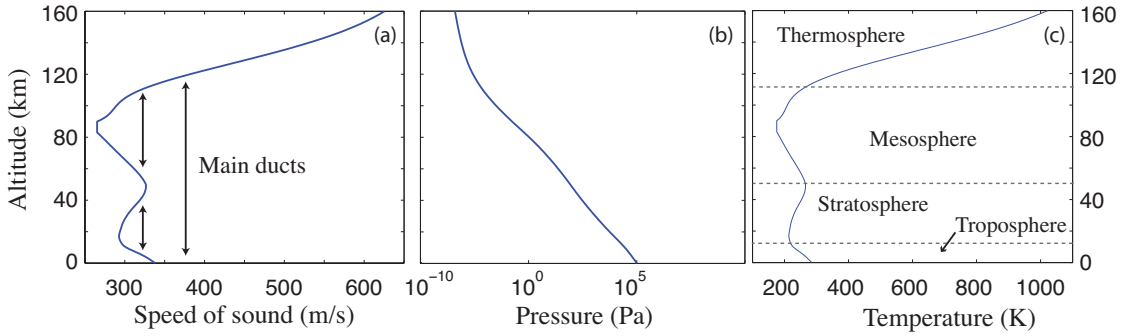

Figure 2.2. Atmospheric profiles of (a) speed of sound, (b) pressure, (c) temperature according to model by *Sutherland and Bass* [2004].

- Temperature ducts: The strong increase in temperature at high thermospheric altitudes results in an increase of the acoustic cut-off frequency, thus limiting upward propagation of infrasound at high altitude. Additionally, the stratospheric temperature inversion creates ducts in the troposphere and stratosphere (see Figure 2.2(a)).

2.4 Acoustic Absorption

The last important atmospheric parameter that needs to be investigated is the absorption of sound through the atmosphere. It is a very difficult parameter to obtain and its values are still controversial. To understand the reason of that complexity, one has to understand the mechanisms of sound absorption in the atmosphere. The theory of sound absorption shows that there are two main mechanisms [*Bass and Sutherland*, 1984]:

- *Classical losses*: the translational (kinetic) energy is converted into equivalent heat energy.
- *Relaxation losses*: the translational energy of the wave is transfered into internal energy of air constituent molecules.

According to *Bass and Sutherland* [1984], at frequencies under 10 MHz, the different contribution to absorption are additive. The model we implement uses that aspect to break absorption into its two main contributions. Details of that

model can be found in [*Sutherland and Bass*, 2004]. The different contributions to absorption are illustrated in Figure 2.3. The first aspect to be noticed is the frequency dependence of the absorption coefficient: high frequencies are going to be absorbed much faster than low frequencies. As a result the atmosphere can be treated as a low pass filter for acoustic waves, and this filter will strongly affect infrasound propagation over long distances. The second aspect to be noticed is the different contributions to the global absorption: at low altitude, the vibrational relaxation of the molecules internal energy is the strongest absorption mechanism, whereas at high altitudes classical viscosity is the main absorption mechanism. Additionally, rotational relaxation of the molecules internal energy has a very small influence on total absorption.

The frequency dependence of the absorption makes the coefficients difficult to implement in a FDTD numerical scheme, as this kind of numerical approach only allows for space and time dependence. This would mean that if we were to implement the absorption model as described in [*Sutherland and Bass*, 2004], we would limit our model to monochromatic sources that are of limited practical interest.

To overcome that difficulty we adopt a solution proposed by *de Groot-Hedlin* [2008] to break down the absorption coefficient $\alpha(z)$ as $\beta(z)+\gamma(z)f^2$, where f is the frequency of the acoustic wave, and β and γ are computed using least-square fit on the *Sutherland and Bass* [2004] model for a given frequency range. Details of the algorithm created to implement the decomposition of $\alpha(z)$ are given in Appendix A. Figure 2.4 shows the absorption reconstruction as done by *de Groot-Hedlin* [2008] and as part of the present work. The computed β and γ can then be used for a wide range of frequencies in our numerical model, as will be discussed in the next Chapter.

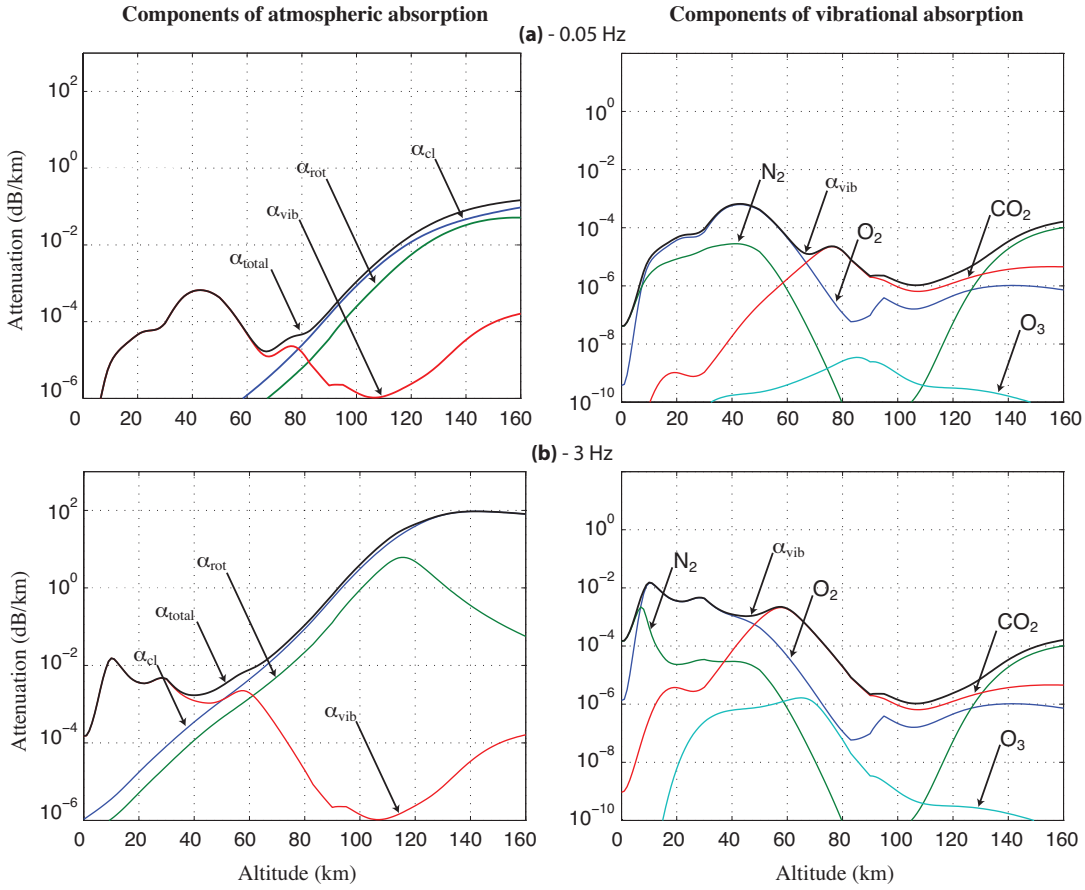

Figure 2.3. Components of the atmospheric absorption coefficient α [dB/km] for frequencies of $f = 0.05$ Hz and $f = 3$ Hz as a function of altitude [*Sutherland and Bass*, 2004]. Left panels show contributions to the total absorption α_{total} from classical diffusion α_{cl}, rotational α_{rot}, and vibrational α_{vib} meachnisms. Right panels detail contributions to the vibrational absorption corresponding to individual molecules O_2, N_2, CO_2 and O_3.

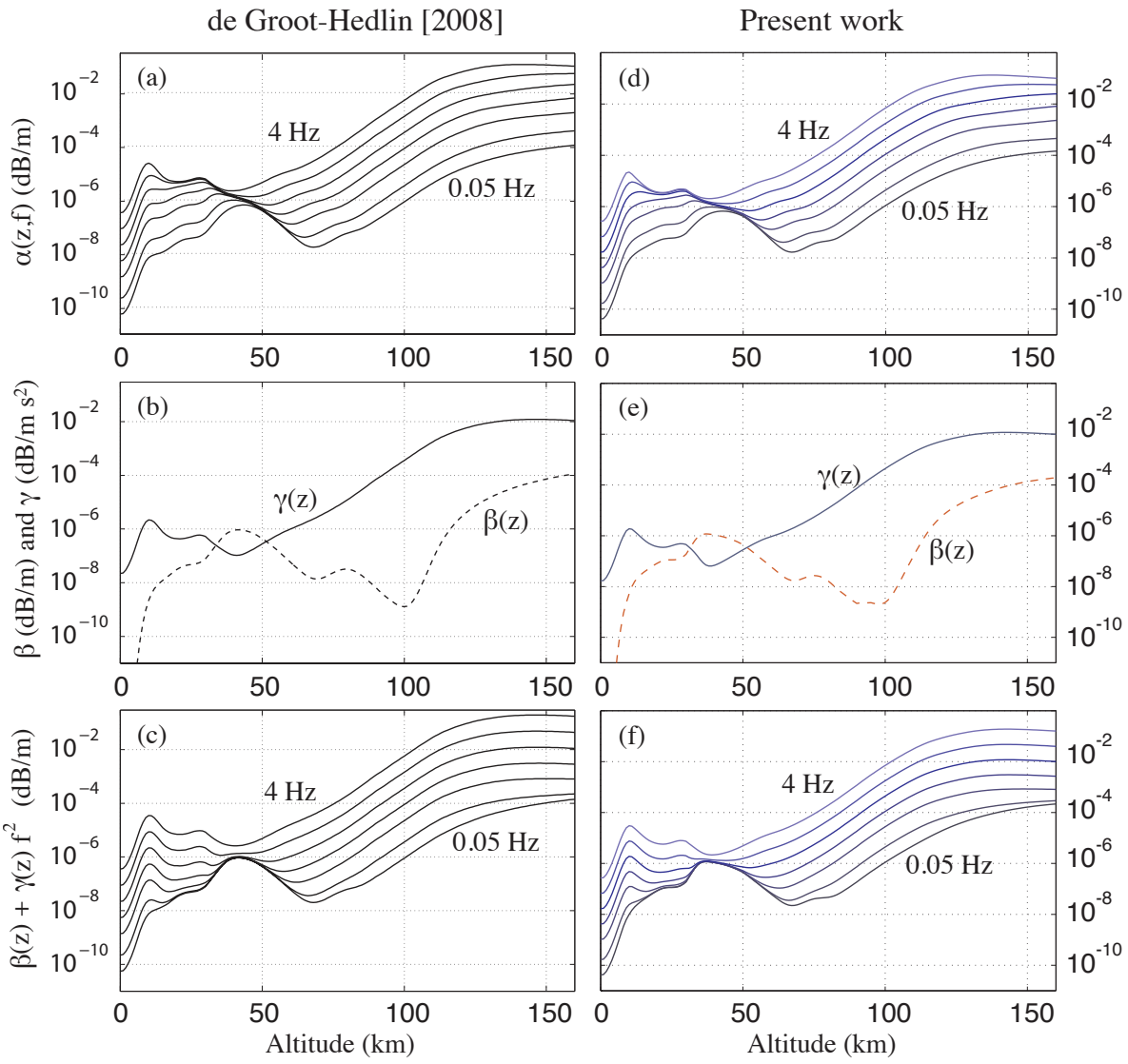

Figure 2.4. Absorption coefficients model. Left panels are adopted from work of *de Groot Hedlin* [2008]. Right panels represent successful reconstruction of the same coefficients obtained as part of the present work. (a) and (d) Absorption coefficient α adopted from *Sutherland and Bass* [2004]; (b) and (e) least square fit; (c) and (f) reconstructed absorption curves.

Chapter 3

Model Implementation

The preliminary work presented in the two previous chapters is implemented in a numerical model. We decided to use the Finite-Difference Time-Domain approach as the best tool to study infrasound propagation over long distances, altitudes and time frames. This chapter presents the details of that numerical implementation.

3.1 Linear Equations

The equations from Chapter 2 are linearized and written in a conservative form as follows:

$$\frac{\partial \tilde{\rho}}{\partial t} + \vec{\nabla} \cdot \rho_0 \vec{v} = 0 \tag{3.1}$$

$$\frac{\partial \tilde{p}}{\partial t} + \vec{\nabla} \cdot c_s^2 \rho_0 \vec{v} = -\rho_0 v_z g \left(\gamma' - 1\right) \tag{3.2}$$

$$\frac{\partial \rho_0 \vec{v}}{\partial t} + \vec{\nabla} \tilde{p} = -\tilde{\rho} \vec{g} + \mu \left(\vec{\nabla}^2 \vec{v} + \frac{1}{3} \vec{\nabla} \left(\vec{\nabla} \cdot \vec{v} \right) \right) - \xi \rho_0 \vec{v} \tag{3.3}$$

where the absorption coefficients μ and ξ have been added to the equations to account for the effects described in the previous chapter. The relations linking μ and ξ to the coefficients β and γ are:

$$\xi(z) \;\; = \;\; 2 c_s \beta(z) \;\; \mathrm{s}^{-1} \tag{3.4}$$

$$\mu(z) \;=\; \frac{3c_s^3\rho_0}{8\pi^2}\gamma(z) \;\; \text{kg/m/s} \tag{3.5}$$

The linearized version of the momentum (3.3) and energy (3.2) conservation equations are obtained by assuming in the original nonlinear equations (Chapter 2) that the quadratic velocity perturbation term $\rho\vec{v}\vec{v}$ can be neglected in comparison with the pressure term p. The assumption of smallness of $\rho\vec{v}\vec{v}$ is always valid for velocity perturbation which remain much lower than the speed of sound $v \ll c_s$, where

$$c_s = \sqrt{\frac{\gamma' p}{\rho}} \;\; \text{m/s} \tag{3.6}$$

This system of partial differential equations is conservative and hyperbolic. Different explicit schemes exist to numerically solve that kind of system, such as Leapfrog, Lax or Lax-Wendrof [*Potter*, 1973]. The choice of the scheme is based on a compromise between stability and computational speed. A high order scheme will be very stable even for non-linear equations, but it will run very slowly. On the other hand, a low-order scheme will be very fast to run, but it will lack the accuracy and stability of a high order scheme. We investigated different schemes to finally choose Leapfrog, as described in the next section.

3.2 Leapfrog Scheme

The Leapfrog scheme is a second order in time and second order in space difference scheme [*Potter*, 1973, p. 65-67]. In one dimension, the scheme could be represented as in Figure 3.1, and in two dimensions as in Figure 3.2. Figure 3.1 allows for a time dimension to be shown, which could not be easily illustrated for the 2-D case. The 2-D solutions are considered in a cylindrical azimuthally symmetric (r, z) simulation domain. It should be noted that absorption terms are not included in the Leapfrog scheme and are implemented through a separate algorithm as will be illustrated bellow. It is important to notice that pressure/density and velocity components are defined on distinctive time/space grids. This process is called a staggered grid: if all points were used to define all of the variables, then there would be two interlocking meshes completely independent of each other due to the

time and space centering of the leapfrog scheme. This would result in a significant slowing of the computation as well as a possible instabilities: due to numerical error propagation, the two meshes may drift out of phase [*Potter*, 1973, pp66]. The space grids have cells dimension of Δr by Δz where $\Delta r = \Delta z$. The variables are sampled in time every Δt: the radial and axial components of velocity v_r and v_z are computed at times $n\Delta t$, and the pressure and density variables $\tilde{\rho}$ and $\tilde{p}$ at times $(n + 1/2)\Delta t$. This time sampling effectively yields discretized difference operators that are accurate to second order.

Adopting the notation:

$$\begin{aligned}
\tilde{\rho}^{n+\frac{1}{2}}_{i,j+1/2} &= \tilde{\rho}\left(i\Delta z, (j+1/2)\Delta r, (n+1/2)\Delta t\right) && (3.7)\\
\tilde{p}^{n+\frac{1}{2}}_{i,j+\frac{1}{2}} &= \tilde{p}\left(i\Delta z, (j+1/2)\Delta r, (n+1/2)\Delta t\right) && (3.8)\\
v^{n}_{r,i,j} &= v_r\left(i\Delta z, j\Delta r, n\Delta t\right) && (3.9)\\
v^{n}_{z,i+\frac{1}{2},j+\frac{1}{2}} &= v_z\left((i+1/2)\Delta z, (j+1/2)\Delta r, n\Delta t\right) && (3.10)
\end{aligned}$$

equations (3.1), (3.3), (3.2) and (3.14) can be discretized as follows:

$$\begin{aligned}
\tilde{\rho}^{n+\frac{1}{2}}_{i,j+\frac{1}{2}} &= \tilde{\rho}^{n-\frac{1}{2}}_{i,j+\frac{1}{2}}\\
&\quad -\frac{\Delta t}{\Delta z}\left(\rho_{0,i+\frac{1}{2}} v^{n}_{z,i+\frac{1}{2},j+\frac{1}{2}} - \rho_{0,i-\frac{1}{2}} v^{n}_{z,i-\frac{1}{2},j+\frac{1}{2}}\right)\\
&\quad -\frac{\Delta t}{\Delta r}\rho_{0,i}\left(v^{n}_{r,i,j+1} - v^{n}_{r,i,j-1}\right)\\
&\quad -\Delta t \rho_{0,i}\frac{\left(v^{n}_{r,i,j+1} + v^{n}_{r,i,j-1}\right)}{2r_{j+\frac{1}{2}}} && (3.11)\\
\tilde{p}^{n+\frac{1}{2}}_{i,j+\frac{1}{2}} &= \tilde{p}^{n-\frac{1}{2}}_{i,j+\frac{1}{2}}\\
&\quad -\frac{\Delta t}{\Delta z}\left(c^2_{s,i+\frac{1}{2}}\rho_{0,i+\frac{1}{2}} v^{n}_{z,i+\frac{1}{2},j+\frac{1}{2}} - c^2_{s,i-\frac{1}{2}}\rho_{0,i-\frac{1}{2}} v^{n}_{z,i-\frac{1}{2},j+\frac{1}{2}}\right)\\
&\quad -\frac{\Delta t}{\Delta r} c^2_{s,i}\rho_{0,i}\left(v^{n}_{r,i,j+1} - v^{n}_{r,i,j-1}\right)\\
&\quad -\Delta t c^2_{s,i}\rho_{0,i}\frac{\left(v^{n}_{r,i,j+1} + v^{n}_{r,i,j-1}\right)}{2r_{j+\frac{1}{2}}}
\end{aligned}$$

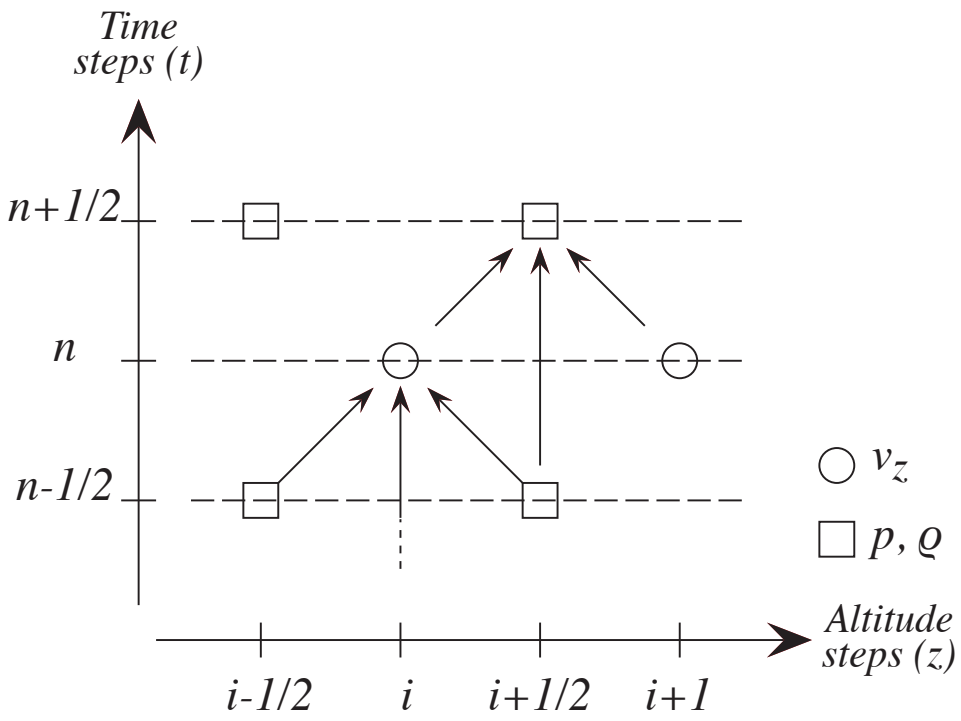

Figure 3.1. The lattice of points in the $z-t$ plane used for second order accuracy in one-dimensional (1-D) implementation of the conservative Leapfrog method [*Potter*, 1973, p. 65-67].

$$-\Delta t g\left(\gamma-1\right)\frac{\left(\rho_{0,i+\frac{1}{2}}v^{n}_{z,i+\frac{1}{2},j+\frac{1}{2}}+\rho_{0,i-\frac{1}{2}}v^{n}_{z,i-\frac{1}{2},j+\frac{1}{2}}\right)}{2} \tag{3.12}$$

$$\begin{aligned}\rho_{0,i+\frac{1}{2}}v^{n+1}_{z,i+\frac{1}{2},j+\frac{1}{2}} &= \rho_{0,i+\frac{1}{2}}v^{n}_{z,i+\frac{1}{2},j+\frac{1}{2}} \\ &\quad -\frac{\Delta t}{\Delta z}\left(\tilde{p}^{n+\frac{1}{2}}_{i+1,j+\frac{1}{2}}-\tilde{p}^{n+\frac{1}{2}}_{i,j+\frac{1}{2}}\right) \\ &\quad -g\Delta t\frac{\left(\tilde{\rho}^{n}_{i+1,j+\frac{1}{2}}+\tilde{\rho}^{n}_{i,j+\frac{1}{2}}\right)}{2}\end{aligned} \tag{3.13}$$

$$\begin{aligned}\rho_{0,i}v^{n+1}_{r,i,j} &= \rho_{0,i}v^{n}_{r,i,j} \\ &\quad -\frac{\Delta t}{\Delta r}\left(\tilde{p}^{n+\frac{1}{2}}_{i,j+\frac{1}{2}}-\tilde{p}^{n+\frac{1}{2}}_{i,j-\frac{1}{2}}\right)\end{aligned} \tag{3.14}$$

The absorption effects are added after each Leapfrog time step through the following algorithm. The Leapfrog scheme stepped variables by Δt to solve for the conservative no absorption case; we then step twice by $\Delta t/2$ to solve for the absorption equation. This approach effectively removes the time centering of the

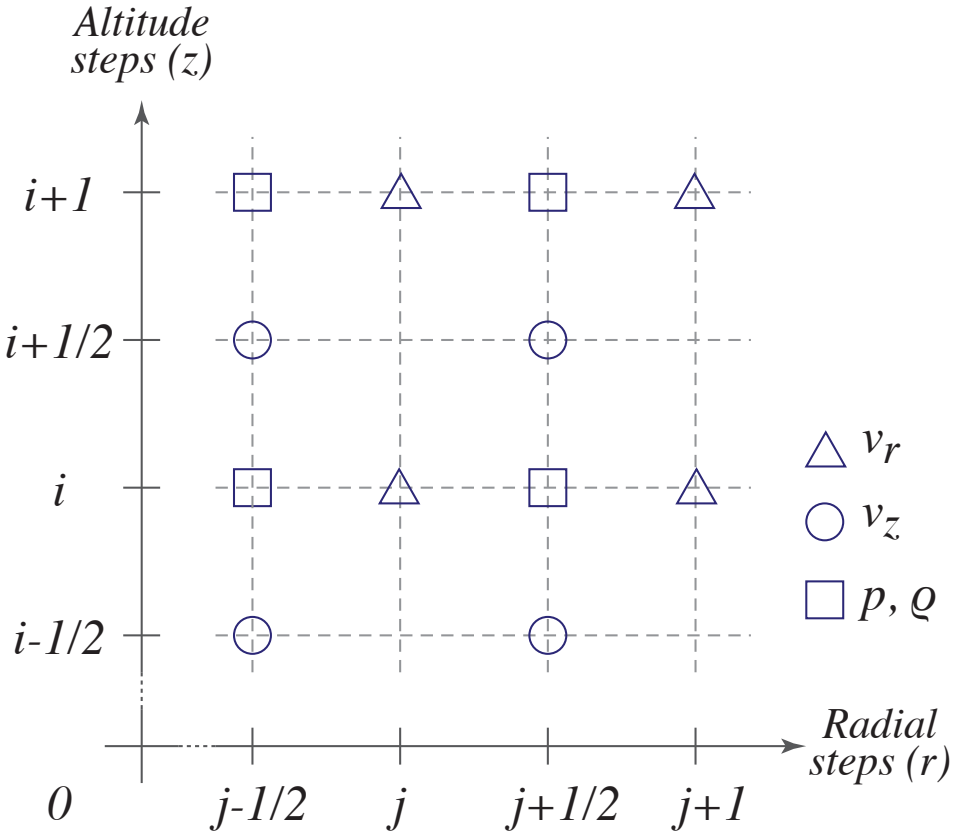

Figure 3.2. The lattice of points in the $r - z$ plane used for second order accuracy in two-dimensional (2-D) implementation of the conservative leapfrog method [*Potter*, 1973, p. 65-67].

numerical schemes, effectively leading to a first order scheme in time. In addition, for second order derivatives, Leapfrog and first order schemes are identical so that the scheme employed to solve for diffusion is an explicit first order scheme in space and time. The reason for not using Leapfrog scheme for the diffusion is that it is unconditionally unstable for diffusion equations [*Potter*, 1973, p. 79]. The equations below show the discretization of the diffusion equation.

$$\begin{aligned} \rho_{0,i} v_{r,i,j}^{n+1} &= \rho_{0,i} v_{r,i,j}^{n+1} \\ &\quad -\frac{\Delta t}{2}\left(F_r^{v_r} + F_{rr}^{v_r} + F_{zz}^{v_r} + F_{rz}^{v_r} + RHS^{v_r}\right) \end{aligned} \tag{3.15}$$

$$\rho_{0,i+\frac{1}{2}} v_{z,i+\frac{1}{2},j+\frac{1}{2}}^{n+1} = \rho_{0,i+\frac{1}{2}} v_{z,i+\frac{1}{2},j+\frac{1}{2}}^{n+1} \tag{3.16}$$

$$-\frac{\Delta t}{2}\left(F_z^{v_z}+F_r^{v_z}+F_{rr}^{v_z}+F_{zz}^{v_z}+F_{rz}^{v_z}+RHS^{v_z}\right)$$

where

$$F_r^{v_r} = \frac{4}{3}\frac{\mu_i}{r_j}\frac{\left(v_{r,i,j+1}^{n+1}-v_{r,i,j-1}^{n+1}\right)}{2\Delta r} \tag{3.17}$$

$$F_{rr}^{v_r} = \frac{4}{3}\mu_i\frac{v_{r,i,j+1}^{n+1}-2v_{r,i,j}^{n+1}+v_{r,i,j-1}^{n+1}}{(\Delta r)^2} \tag{3.18}$$

$$F_{zz}^{v_r} = \mu_i\frac{v_{r,i+1,j}^{n+1}-2v_{r,i,j}^{n+1}+v_{r,i-1,j}^{n+1}}{(\Delta z)^2} \tag{3.19}$$

$$F_{rz}^{v_r} = \frac{\mu_i}{3}\left(\frac{v_{z,i+\frac{1}{2},j+\frac{1}{2}}^{n+1}-v_{z,i+\frac{1}{2},j-\frac{1}{2}}^{n+1}}{\Delta r\Delta z}-\frac{v_{z,i-\frac{1}{2},j+\frac{1}{2}}^{n+1}-v_{z,i-\frac{1}{2},j-\frac{1}{2}}^{n+1}}{\Delta r\Delta z}\right) \tag{3.20}$$

$$RHS^{v_r} = \xi_i\rho_{0,i}v_{r,i,j}^{n+1}-\frac{4}{3}\mu_i\frac{v_{r,i,j}^{n+1}}{r_j} \tag{3.21}$$

$$F_z^{v_z} = \frac{\mu_i}{3r_j}\left(\frac{v_{r,i+1,j+1}^{n+1}+v_{r,i+1,j}^{n+1}}{2}-\frac{v_{r,i,j+1}^{n+1}+v_{r,i,j}^{n+1}}{2}\right)\frac{1}{\Delta z} \tag{3.22}$$

$$F_r^{v_z} = \frac{\mu_i}{r_j}\frac{v_{z,i+\frac{1}{2},j+\frac{3}{2}}^{n+1}-v_{z,i+\frac{1}{2},j-\frac{1}{2}}^{n+1}}{2\Delta r} \tag{3.23}$$

$$F_{rr}^{v_z} = \mu_i\frac{v_{z,i+\frac{1}{2},j+\frac{3}{2}}^{n+1}-2v_{z,i+\frac{1}{2},j+\frac{1}{2}}^{n+1}+v_{z,i+\frac{1}{2},j-\frac{1}{2}}^{n+1}}{(\Delta r)^2} \tag{3.24}$$

$$F_{zz}^{v_z} = \frac{4}{3}\mu_i\frac{v_{z,i+\frac{3}{2},j+\frac{1}{2}}^{n+1}-2v_{z,i+\frac{1}{2},j+\frac{1}{2}}^{n+1}+v_{z,i-\frac{1}{2},j+\frac{1}{2}}^{n+1}}{(\Delta z)^2} \tag{3.25}$$

$$F_{rz}^{v_z} = \frac{\mu_i}{3}\left(\frac{v_{r,i+1,j+1}^{n+1}-v_{r,i+1,j}^{n+1}}{\Delta r\Delta z}-\frac{v_{r,i,j+1}^{n+1}-v_{r,i,j}^{n+1}}{\Delta r\Delta z}\right) \tag{3.26}$$

$$RHS^{v_z} = \xi_i\rho_{0,i}v_{z,i+\frac{1}{2},j+\frac{1}{2}}^{n+1} \tag{3.27}$$

To achieve stability in the numerical model, we have to respect the following criteria [e.g., *Potter*, 1973, p. 67, p. 79]:

$$\Delta t \leq \frac{\Delta z}{c_s\sqrt{2}} \tag{3.28}$$

$$\Delta t \leq 0.5\frac{(\Delta z)^2}{\kappa} \tag{3.29}$$

$$0 < \xi \Delta t \leq 1 \tag{3.30}$$

where $\kappa = (4/3)(\mu/\rho_0)$ and we assumed that $\Delta r{=}\Delta z$

3.3 Artificial Viscosity

Intrinsically the Leapfrog scheme is a high-order scheme that produces small amplitude high frequency perturbations that can be amplified by numerical dispersion and/or boundary reflections. For the purpose of removing related short wavelength oscillations we introduce an artificial viscosity [e.g., *Sparrow and Raspet*, 1991] $\mu_{art} = \nu_{art}\frac{(\Delta z)^4}{\Delta t}$ with $\nu_{art} = 0.05$ in equation (3.3):

$$\frac{\partial \rho_0 \vec{v}}{\partial t} + \vec{\nabla}\tilde{p} \;=\; -\tilde{\rho}\vec{g} + \mu\left(\vec{\nabla}^2\vec{v} + \frac{1}{3}\vec{\nabla}\left(\vec{\nabla}\cdot\vec{v}\right)\right) - \xi\rho_0\vec{v} - \mu_{art}\frac{\partial^4 v_z}{\partial z^4} \tag{3.31}$$

The artificial viscosity is implemented after each Leapfrog and absorption steps using the following algorithm:

$$\begin{aligned} v^{n+1}_{r,i,j} &= v^{n+1}_{r,i,j} \qquad (3.32)\\ &\quad +\nu_{art}\left(v^{n+1}_{r,i,j+2} - 4v^{n+1}_{r,i,j+1} + 6v^{n+1}_{r,i,j} - 4v^{n+1}_{r,i,j-1} + v^{n+1}_{r,i,j-2}\right)\\ v^{n+1}_{z,i+\frac{1}{2},j+\frac{1}{2}} &= v^{n+1}_{z,i+\frac{1}{2},j+\frac{1}{2}} \qquad (3.33)\\ &\quad +\nu_{art}\left(v^{n+1}_{z,i+\frac{5}{2},j+\frac{1}{2}} - 4v^{n+1}_{z,i+\frac{3}{2},j+\frac{1}{2}} + 6v^{n+1}_{z,i+\frac{1}{2},j+\frac{1}{2}} - 4v^{n+1}_{z,i-\frac{1}{2},j+\frac{1}{2}} + v^{n+1}_{z,i-\frac{3}{2},j+\frac{1}{2}}\right) \end{aligned}$$

The artificial viscosity doesn't affect the propagating wave. It only smoothes down the small high frequency (short wavelength) perturbations introduced by the numerical scheme. One downside of artificial viscosity though is that it increases the computation time of the model.

3.4 Boundary Conditions

In two dimensional studies, we investigate vertical and radial propagating waves. This requires three specific kinds of boundary conditions for our simulation domain:

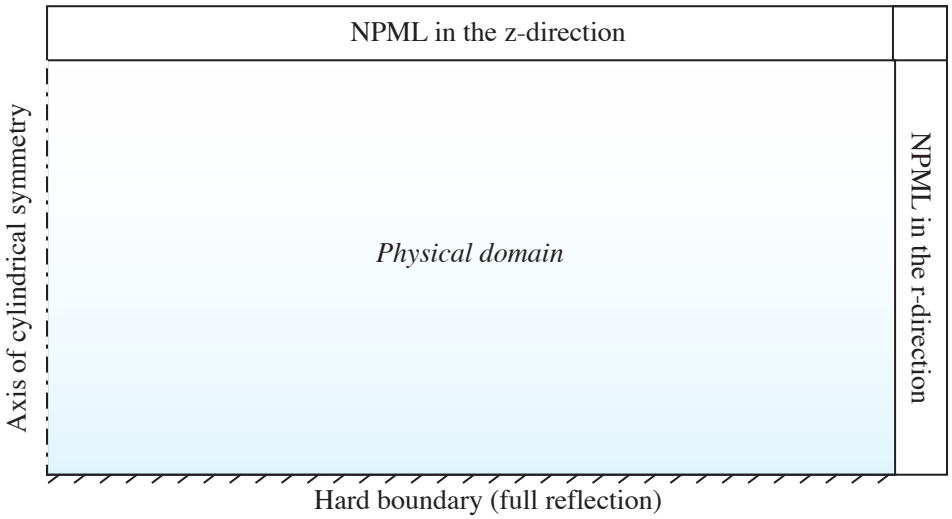

Figure 3.3. Cross sectional view of the model domain illustrating the different boundaries implemented in the numerical modeling of acoustic wave propagation.

- the lower boundary should be reflective (ideal case of a smooth and reflective ground).
- the left boundary is our axis of symmetry.
- the top and right boundary should be opened as we want the waves to keep propagating past the numerical domain without generating non-physical reflections.

Figure 3.3 illustrates the boundary conditions described in this section.
The reflective boundary is enforced as follows [e.g., *Sparrow and Raspet*, 1991]:

$$v^n_{r,i=0,j} = v^n_{r,i=1,j} \tag{3.34}$$

$$v^n_{z,i=0,j} = -v^n_{z,i=1,j} \tag{3.35}$$

$$\tilde{\rho}^n_{z,j=0} = \tilde{\rho}^n_{z,j=1} \tag{3.36}$$

$$\tilde{p}^n_{z,j=0} = \tilde{p}^n_{z,j=1} \tag{3.37}$$

The axis boundary is more complex as gradients in cylindrical coordinates have $1/r$ dependencies. In practical implementation L'Hospital's rule is applied to solve

for the fluxes on the axis. In addition we enforce the following condition for the radial velocity on the axis $v^n_{r,i,j=0} = 0$ due to the symmetry.

The open boundary requires very careful numerical manipulations. One intuitive way of doing it would be to neglect the change between the two last points of the domain. This will however generate a small reflection that can then be amplified due to atmospheric pressure scaling. One way to compensate for it is to artificially decrease the speed of sound in the upper layer of the atmosphere (above 160 km); this will result in a decrease in the wavelength of the waves going through that medium, thus increasing greatly the effect of absorption on those waves (because absorption is proportional to the frequency squared). This is not a problem for the physical propagation of the wave since at those altitudes most of the infrasound have already been absorbed, and the remaining waves are mostly due to unwanted reflection. However, this method is not optimal as it requires a large artificial layer where the waves can be slowly damped.

An alternative is to implement a Perfectly Matched Layer (PML) absorbing boundary condition: this numerical technique has been introduced by *Berenger* [1994] for electromagnetic waves. In the FDTD model presented in this thesis, we implement a variant of Berenger's PML called a Nearly Perfectly Matched Layer [*Cummer*, 2003; *Hu et al.*, 2007]. An additional thin layer is designed where the gradient in the opening direction (z-direction for the top boundary and r-direction for the right boundary) is modified as follows:

$$\partial\alpha \implies \partial\tilde{\alpha} = \left(1 - j\frac{\eta(\alpha)}{\omega}\right)\partial\alpha \tag{3.38}$$

where $\alpha = \{r, z\}$ for the right and top boundary respectively, and

$$\eta(\alpha) = \begin{cases} \eta_m \left(\frac{\alpha - \alpha_{lim} - L_{npml}}{L_{npml}}\right)^3 & \text{when } \alpha \geq \alpha_{lim} \\ 0 & \text{otherwise} \end{cases}$$

where η_m is chosen empirically to absorb waves in the NPML medium (typically $\sim$20 for the considered frequency range), α_{lim} is the limit of the physical domain in r or z direction, and L_{npml} is the thickness of the NPML medium. This creates a new set of equations for the PML layers. In particular, for the top PML layer we have:

$$\frac{\partial \tilde{p}^z}{\partial z} + \frac{\partial \rho_0 v_z}{\partial t} = 0 \tag{3.39}$$

$$\frac{\partial c_s^2 \rho_0 v_r}{\partial r} + \frac{c_s^2 \rho_0 v_r}{r} + \frac{\partial c_s^2 \rho_0 v_z^z}{\partial z} + \frac{\partial \tilde{p}}{\partial t} = 0 \tag{3.40}$$

$$\frac{\partial F^z}{\partial t} + \eta(z) = \frac{\partial F}{\partial t} \quad \text{where } F = \{\tilde{p}, v_z\} \tag{3.41}$$

The boundary is then solved for in the following order: equation (3.40) is used to update $\tilde{p}$, then equation (3.41) can be used to find the auxiliary variable $\tilde{p}^z$, and finally v_z is updated using equation (3.39). The last step is to find the other auxiliary variable v_z^z using equation (3.41). The exact same process is repeated for the right boundary, this time using the auxiliary variable $\tilde{p}^r$ and v_r^r. Finally, in the upper right corner of the domain, both NPML equation sets are implemented.

3.5 Parallel Implementation

For obvious computational time considerations, a parallel implementation of the code is a strong advantage [e.g, *Pacheco*, 1996; *Gropp*, 1999]. However, when modeling infrasound in the atmosphere, the main problem is the size of the domain. For instance, a simulation domain with 160 km vertical by 100 km radial extent may require considerable amount of memory depending on the highest frequency represented: a frequency of 5 Hz requires a spatial resolution of at least 6 m to maintain ten grid points per wavelength. Since the model computes the two components of velocity, pressure and density perturbation, four matrices are needed to represent the full simulation domain: this means that the code, while running, needs 160×10^3 [m]/6 [m] $\times$ 100×10^3 [m]/6 [m] $\times$ 4 [matrices] $\times$ 8 [bytes] = 13.2 [GigaBytes]. Very few systems provide that amount of physical memory for a single user. In order to avoid limitations in the resolution as well as in the simulation domain size, a parallel code with memory distribution is required.

The strategy used for our model is to split the domain into horizontal layers. Each processor computes the solutions for a given horizontal layer and at the end of each time step sends its upper and lower row of grid points to the upper and lower layers respectively. These rows are received in what are called “ghost

rows" in the neighboring layers. Such a manipulation is possible using the Message Passing Interface (MPI) with only minor modifications to the code: exceptions for the upper and bottom layers have to be implemented, and structures have to be designed to efficiently communicate between the processors. This implementation allows for a minimal exchange of information between the processors and does not require to gather all the information on a single processor, thus providing the necessary memory distribution.

Tests have been performed on a Penn State cluster [lionXI, *High Performance Computing Group*, http://rcc.its.psu.edu/hpc/] to evaluate the performance of the parallel code. Results are presented in Figure 3.4 and show a nearly linear increase of the computational speed. Although Figure 3.4 shows results up to 20 processors, the code has been tested with up to 64 processors on a different Penn State cluster [lionXK, *High Performance Computing Group*] indicating a similar trend in performance increase.

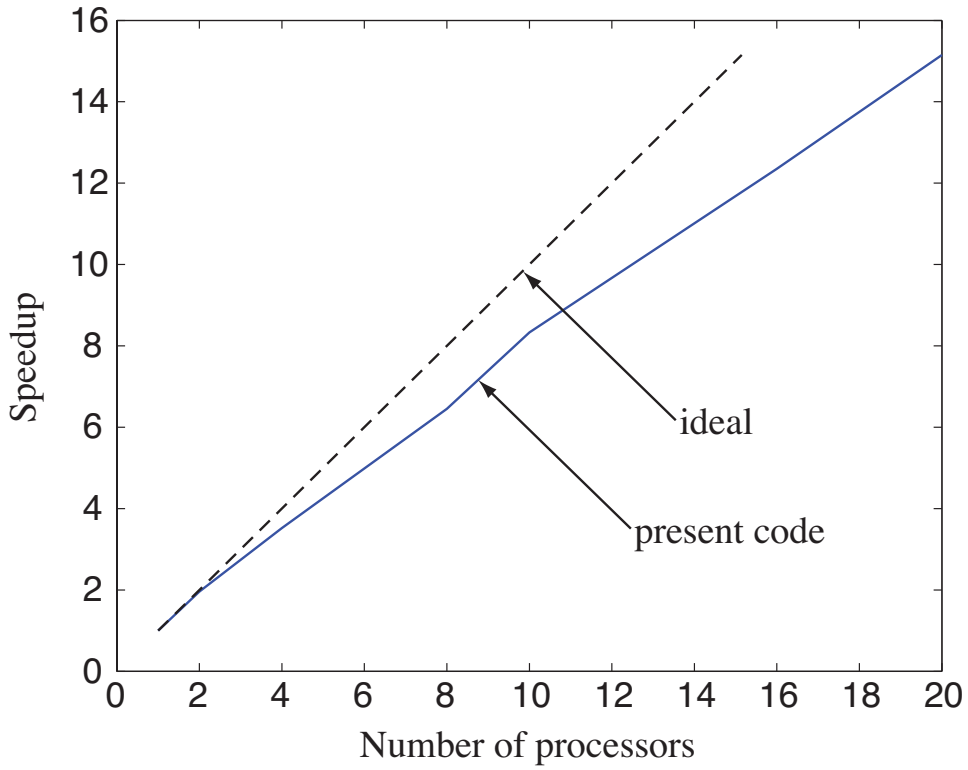

Figure 3.4. Factor of increase in computational speed versus number of processors with a fixed number of grid points. The ideal case represents the expected speedup if there was no time expenditure related to communication between processors.

Chapter 4

Modeling of Infrasonic Signals from Pulsating Auroras

4.1 Observations of Infrasonic Emissions from Pulsating Auroras

Recently, *Wilson et al.* [2005] reported infrasonic signatures attributed to pulsating auroras observed by the infrasonic array I53US in Fairbanks, Alaska. Pulsating auroras are reported to have horizontal extents of 10 to 200 km [*Jones et al.*, 2009], vertical extents of 2 to 25 km [*Jones et al.*, 2009; *Stenbaek-Nielsen and Hallinan*, 1979], and a pulse repetition period ranging from 1 to 40 s [*Johnstone*, 1978]. Infrasound signatures from pulsating auroras are attributed to the precipitation energetic flux particles into the upper atmosphere [e.g., *Maeda and Watanabe*, 1964; *Wilson et al.*, 2005; *Johnstone*, 1978]. The precipitation of energy is estimated using spectroscopic data from pulsating auroras and typically ranges from a few erg cm^{-2} s^{-1} (1 erg cm^{-2} s^{-1} = 10^{-3} J m^{-2} s^{-1}) for weak pulsating auroras to 10-20 erg cm^{-2} s^{-1} for more energetic auroras, with a maximum of 25 erg cm^{-2} s^{-1} [*Davidson and Sears*, 1980].

Although the morphology of pulsating auroral forms is well documented, the exact physical mechanisms of pulsating aurora still remain a subject of active debate [*Jones et al.*, 2009, and references therein]. The frequency domain coherence between the luminous intensity of the pulsating aurora and the infrasound received

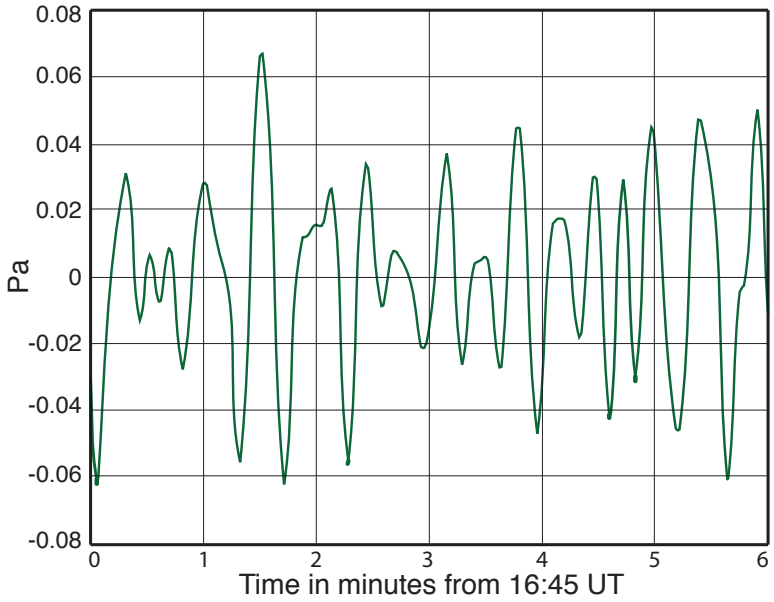

Figure 4.1. Best beam infrasonic data at I53US from 16:45 to 16:51 on day 349, 2003. Average of the waveforms that were band-pass filtered between 0.02 and 0.10 Hz [*Wilson et al.*, 2005].

at the Earth surface have been investigated in [*Wilson et al.*, 2005; *Wilson and Olson*, 2005]. Video data of a pulsating aurora from an All-Sky video camera on the night of December 5, 2003 was compared with the pressure waveform data from the infrasonic array I53US at Fairbanks, Alaska. Enhanced coherence between the two signals was observed when a propagation delay time for the infrasound sample with respect to the video data sample was used. The required 5 to 6 minutes lag was consistent with the expected downward propagation time for waves from a source near 110 km altitude. The frequency domain coherence was found to be high between the pulsating aurora intensity above the array and the high trace-velocity infrasound signals at the surface in the pass band from 0.03 to 0.08 Hz. Ray-tracing studies indicate that such high trace-velocity infrasound signals originate from sources within 35 km of the zenith above the array for a source height of 110 km. The high coherence between the video and infrasound data led authors to believe that periodic heating of the atmosphere by pulsating aurora is the source of the observed infrasound [*Wilson et al.*, 2005; *Wilson and Olson*, 2005]. Figure 4.1 shows the infrasonic signals observed in coherence with the video data of the pulsating auroras.

4.2 Modeling Results

The infrasonic source is modeled as a cylindrical layer of thickness h_s and radius R_s with lower boundary positioned at an altitude z_s as illustrated in Figure 4.2. In the 1-D model, the cylindrical source converts into a slab of infinite horizontal extent. We assume that the precipitating particle energy flux F_s (in erg/cm^2/s or J/m^2/s) is entirely converted into heat inside the cylinder during a given time τ_s. The distribution of that energy is assumed to decrease exponentially with height so that most of the energy is deposited toward the lower boundary of the source. The corresponding heat source can be expressed as follows:

$$q(z,t) = (F_s/h_s)\, e^{-(z-z_s)/h_s} \mathrm{J/m^3/s},\ t \leq \tau_s \tag{4.1}$$

The resulting pressure perturbation is derived from the first law of thermodynamics and included in the energy conservation equation as:

$$\tilde{p} = (\gamma' - 1)q \tag{4.2}$$

where γ' is the ratio of specific heats [*Maeda and Watanabe*, 1964].

Both the 1-D and 2-D models are run using a value of the flux F_s of 5 erg/cm^2/s as suggested in [*Johnstone*, 1978], and a heating time of τ_s=20 s as suggested in [*Royrvik and Davis*, 1977].

The 2-D model is run for a source of vertical extent h_s=8 km with its lower boundary at z_s=100 km altitude and a radius R_s=50 km. Results in Figure 4.3 are presented in terms of normalized pressure perturbation $\tilde{p}/p_0(z)\sqrt{p_0(z)/p_0(z_s)}$. Figure 4.3(a) shows results from the 2-D model 360 seconds after initiation of the source. An observer on the ground placed anywhere from 0 to around 50 km from the axis would see a plane wave. Figure 4.3(b) compares the 2-D and 1-D model results at three instants in time, t=20, 160 and 340 s. The pressure perturbation from the 2-D model is measured on the axis of the domain. There is a very good agreement between 1-D and 2-D models, thus suggesting that the use of the 1-D model is fully sufficient for this study, in agreement with similar conclusions reached in [*Wilson et al.*, 2005]. Unless mentioned otherwise, all results presented hereafter will be extracted from the 1-D model calculations.

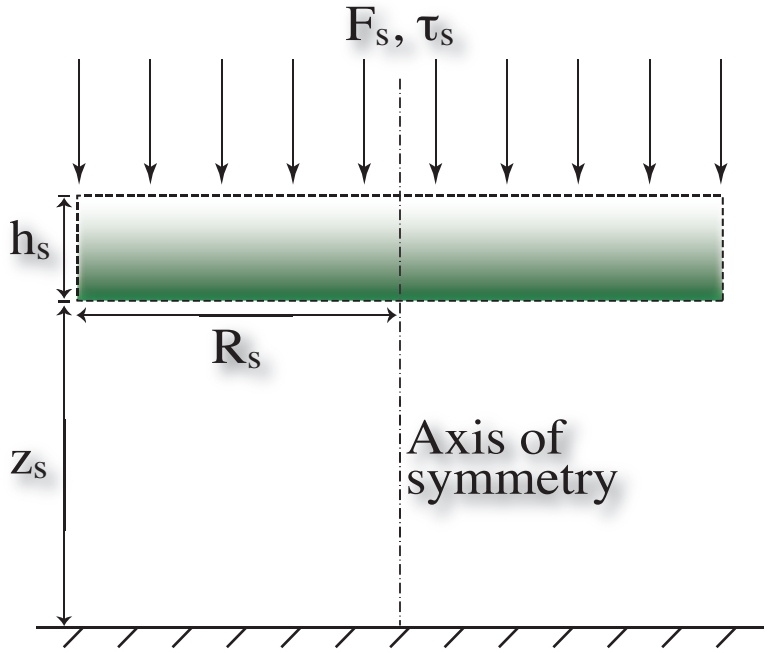

Figure 4.2. Cross-sectional view of the model domain illustrating the parameters and geometry of the model.

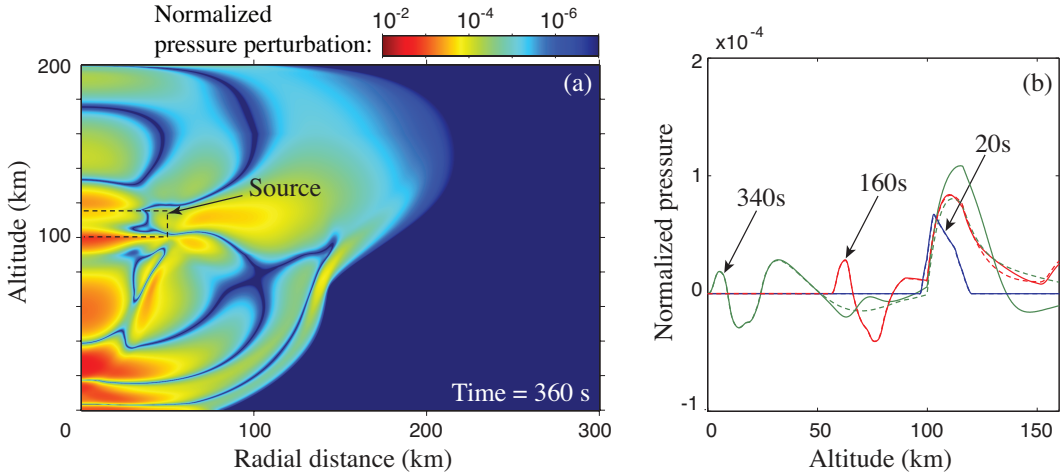

Figure 4.3. (a) Normalized magnitude of pressure perturbation obtained from the 2-D model for an h_s=8 km thick source with z_s=100 km observed at time 360 s. (b) Comparison between 1-D (solid lines) and 2-D (dashed lines) models at times 20, 120 and 340 s.

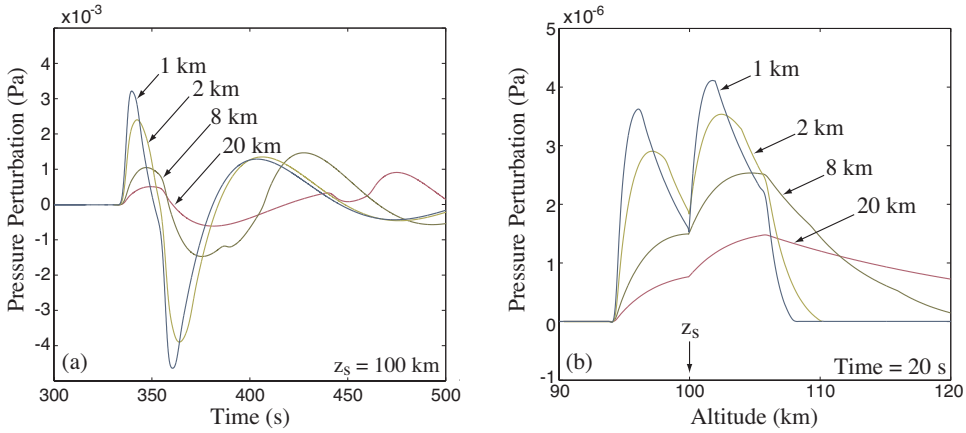

Figure 4.4. Comparison between model results obtained for different source vertical extents h_s. (a) Pressure perturbation observed on the ground for 4 different vertical extents of a source with $z_s = 100$ km. (b) Pressure perturbation at the end of the source excitation at time $t = \tau_s$=20 s.

The influence of the source vertical extent on pressure perturbation observed on the ground is illustrated in Figure 4.4 for sources of vertical extent h_s=1, 2, 8 and 20 km with a lower boundary set at z_s=100 km. Figure 4.4(a) evidences that the smaller the vertical extent, the higher the observed amplitude is. The same observation can be made from Figure 4.4(b): after t=τ_s=20 s, when all the energy has been deposited in the source volume, the pressure wave amplitude of the source with the smallest vertical extent is the highest.

In Figure 4.5(a), results for a source of vertical extent h_s=1 km with its lower bound placed at z_s=90, 100, 110, 120, 130, 140, 150 and 155 km altitude are presented. A similar analysis is conducted for sources with vertical extents h_s=2 and 8 km. It appears that an increased source altitude leads to an increased observed pressure perturbation on the ground up to a given limit marked by a star in Figure 4.5(b). Above that limit, the amplitude of the observed ground pressure wave decreases when the altitude of the source lower boundary increases.

4.3 Discussion

The 2-D model generates pressure perturbation that exhibits a plane wave structure when it reaches the ground, as evidenced by Figure 4.3(a). The source radius R_s=50 km chosen for the present study reasonably illustrates the wave structure

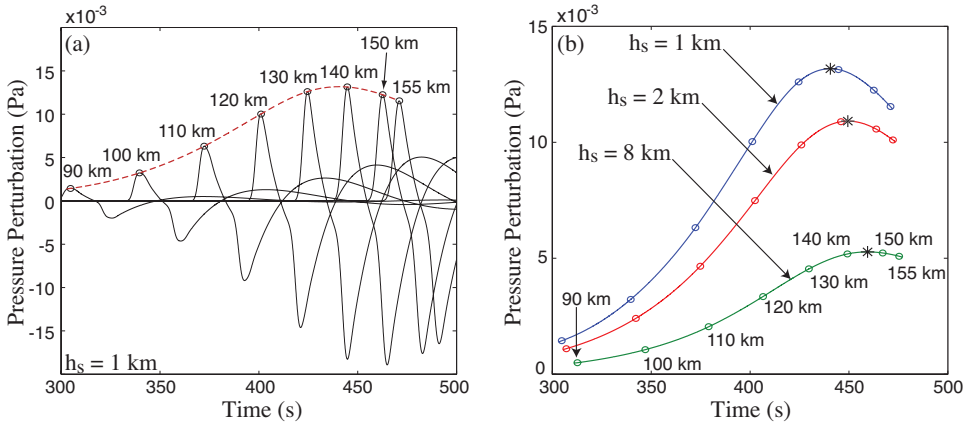

Figure 4.5. Comparison between model results obtained for a source positioned at different altitudes. (a) Pressure perturbation on the ground for a source vertical extent h_s=1 km positioned at altitudes from 90 to 155 km. (b) The same analysis as in (a) for sources with h_s=8, 2 and 1 km.

created by a pulsating aurora. *Jones et al.* [2009, and references therein] report horizontal extents ranging from 10 to 200 km. The horizontal extent of the source relatively to its altitude explains the observed plane wave. Furthermore, the comparison of the pressure perturbation generated by the 1-D and 2-D models in Figure 4.3(b) shows a very good agreement between the two models. The agreement between 1-D and 2-D models is in full accord with observations by *Wilson et al.* [2005] of very high acoustic trace velocities that are characteristic of a plane wave coming from almost straight above the infrasonic array.

The pressure perturbation created by the energy flux through the aurora layer should exhibit a $1/h_s$ dependency related to the assumption that a constant flux of energy is deposited into a variable volume: as the volume is reduced, the energy density has to increase to obtain the same total energy, hence the pressure perturbation amplitude increases [*Maeda and Watanabe*, 1964]. Results presented in Figure 4.4(a) do not, however, exactly reproduce the $1/h_s$ dependency. This difference is the manifestation of the speed of sound effects leading to propagation of the pressure wave outside of the heating volume during the heating time τ_s. At an altitude of z_s=100 km the speed of sound is $c_s \simeq$ 290 m/s, so that for a source at that altitude after 20 s the pressure wave would have propagated almost 6 km. This means that for a source of vertical extent h_s larger than 6 km, we can consider that the energy is deposited almost instantaneously, and the $1/h_s$ dependency would be

respected, whereas for a source smaller than 6 km, the pressure wave propagates outside of the source volume before all the energy has been deposited. Figure 4.4(b) shows that after 20 s, the break in the pressure perturbation curve, located at the lower vertical boundary of the source, is sharper for smaller sources, which indicates that more of the source pressure perturbation has propagated outside of the source volume.

The pressure perturbation for the linear lossless propagation in a stratified atmosphere would scale as the square root of the ambient pressure $\tilde{p} \sim \sqrt{p_0}$ [*Gossard and Hooke*, 1975, p. 77; *Maeda and Watanabe*, 1964]. Figure 4.5(a) illustrates this effect as the observed ground amplitudes increase as the constant vertical extent source is placed at higher altitudes in the atmosphere. The amplification due to gravity stratification is, however, limited by absorption: the higher the source is initiated, the longer the path of the wave through the atmosphere will be. It can also be noticed from the expression of the absorption coefficient α given in Chapter 2 that absorption is proportional to the square of frequency. Since larger sources can be characterized as having a larger wavelength and lower frequency, they will have a higher optimum initial height as shown in Figure 4.5(b), simply reflecting stronger absorption of high frequency waves at higher altitudes in comparison with low frequency waves.

Although a higher source altitude z_s gives us higher wave amplitudes on the ground, only sources between 90 and 110 km altitude fit the 5 to 6 min time lag between visual observation and infrasound measurements for the pulsating aurora observed by *Wilson et al.* [2005]. Pulsating auroras have been observed at altitudes higher than a 110 km [e.g., *Brown et al.*, 1976], but most observations suggest average altitudes between 90 and 110 km [e.g., *Stenbaek-Nielsen and Hallinan*, 1979].

Modeling results presented in this work use heating rates equivalent to a precipitating electron flux F_s=5 erg/cm^2/s. For realistic source altitudes, 90 to 110 km, the resulting modeled pressure perturbations are roughly an order of magnitude smaller than those observed. Hence a source equivalent to a precipitating electron flux of 50 erg/cm^2/s would be needed to obtain a pressure perturbation of 0.05 Pa on the ground. This is in agreement with previous estimates by *Maeda and Watanabe* [1964]. The energy flux of 5 erg/cm^2/s may be too conservative. *Davidson*

and Sears [1980] and *Sears and Vondrak* [1981] have reported values between 10 to 20 erg/cm^2/s based on optical observations for more energetic pulsating auroras, with an observed maximum of 25 erg/cm^2/s. We note that even this observed maximum produces a factor of two lower pressure perturbations than observed, suggesting possible additional sources. A possibility is Joule heating from ionospheric currents modulated by the pulsating aurora. *Weimer* [2005] and *Kosch and Nielsen* [1995] indicate that the energy input from Joule heating is of same order as the particle energy input while *Lu et al.* [1998] find Joule heating to be significantly more important. These studies were done on much larger spatial scales than the individual patches of pulsating auroras we are considering, and it is uncertain whether the same ratios apply here. Nevertheless, Joule heating is likely an important additional energy source, which needs further investigation.

Chapter 5

Modeling of Infrasonic Signatures of Sprites

5.1 Observations of Infrasound Radiations from Sprites

Sprites are large luminous discharges which appear in the altitude range ∼40-90 km above large thunderstorms, typically following intense positive cloud to ground lightning discharges [e.g., *Pasko*, 2007, and extensive list of references therein]. They usually last from a few milliseconds up to a few hundred milliseconds. Recent telescopic imaging of sprites revealed fine structures in these events with transverse spatial scales ranging from a few tens of meters at lower altitudes, up to a few hundreds of meters at higher altitudes [*Gerken and Inan*, 2002]. It has also been demonstrated that sprites often exhibit a sharp altitude transition between the upper diffuse and the lower highly structures region at ∼80 km [*Pasko and Stenbaek-Nielsen*, 2002; *Gerken and Inan*, 2003].

There is a strong experimental evidence that thunderstorms represent significant sources of infrasonic waves [e.g., *Blanc*, 1985; *Drob et al.*, 2003]. Two different mechanisms for generation of infrasound by lightning have been proposed: the radial expansion of a hot lightning channel [*Few*, 1995], and the sudden reduction of the electric field inside a thundercloud immediately following a lightning discharge [e.g., *Wilson*, 1920; *Pasko*, 2009]. Some level of air heating is expected to

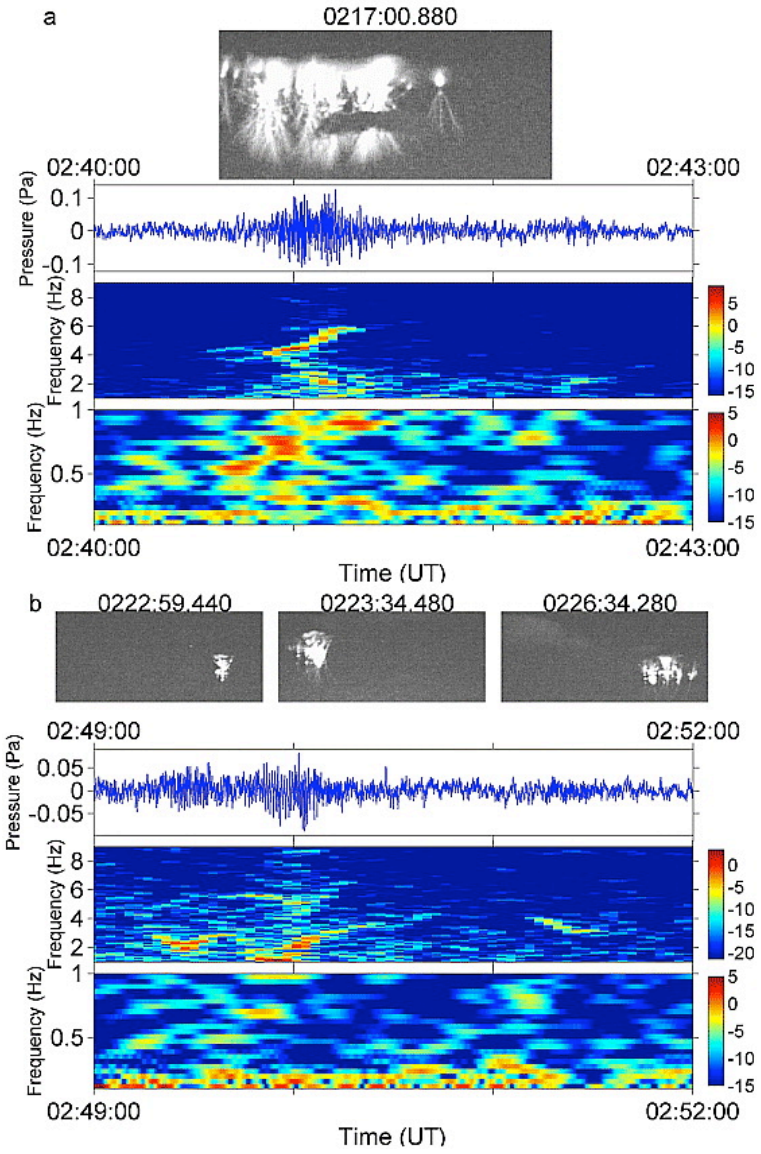

Figure 5.1. Images of sprites and associated infrasound signals. The infrasound spectrograms are given for two ranges 1-9 Hz and 0.1-1 Hz. The color scales are in dB [*Farges et al.*, 2005].

be present in sprites, thus suggesting that it would be interesting to determine the characteristics of infrasound emissions from these events.

The history of research related to infrasound radiation from sprites is relatively short, with most of contributions and publications coming from several European research groups. The possibility of infrasound generation by sprite discharges has been discussed in a presentation at Fall AGU 1999 meeting by *Bedard et al.* [1999].

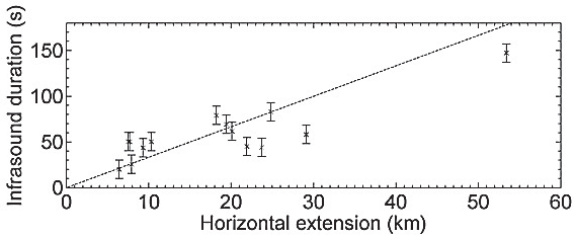

Figure 5.2. Infrasound duration versus horizontal sprite extension [*Farges et al.*, 2005].

Specific chirp-like infrasound signatures possibly related to sprite discharges have been identified by *Liszka* [2004], and their phenomenology further discussed by *Liszka and Hobara* [2006]. *Farges et al.* [2005], reported the first unambiguous infrasound signals generated by sprites from simultaneous observations of infrasound and sprites. Observations reveal that sprites produce chirp-like infrasonic signatures when observed at a distance of ∼400 km, as shown in Figure 5.1. The signatures are characterized by arrival of low frequencies before high frequencies. Measured signals typically last 1-2 minutes with amplitudes of a few 10^{-2} Pa. It should be noticed in Figure 5.1, that duration and amplitude of the infrasonic chirp seems correlated to the horizontal extent of the sprites. Additional measurements by *Farges et al.* [2005] confirm that hypothesis: Figure 5.2 shows a good linear correlation between infrasound signal duration and sprite's horizontal extents. In addition the straight line on Figure 5.2 with a slope equal to the sound speed of 300 m/s suggest that the duration of the infrasonic signal is indeed related to the time necessary for an infrasonic wave to travel from one side of the sprite to the other.

More recently, *Farges and Blanc* [2010], reported observations of very specific infrasonic signatures that could be correlated with sprite events too. Those events are manifested by arrival of high frequencies before low frequencies (i.e., inverted chirps) Those signatures shown in Figure 5.3 appear when monitoring infrasonic signals within a 100 km of a thunderstorm known to produce sprites. Although no direct video captures of sprites can be related to the infrasound signals because the sprites where out of the camera field of view, inverse ray-tracing suggest high altitude sources between 40 and 90 km, which correspond to typical altitudes of sprites. Furthermore, the lightning activity when those infrasound signatures were observed is typical of sprite producing storms and some sprites were indeed

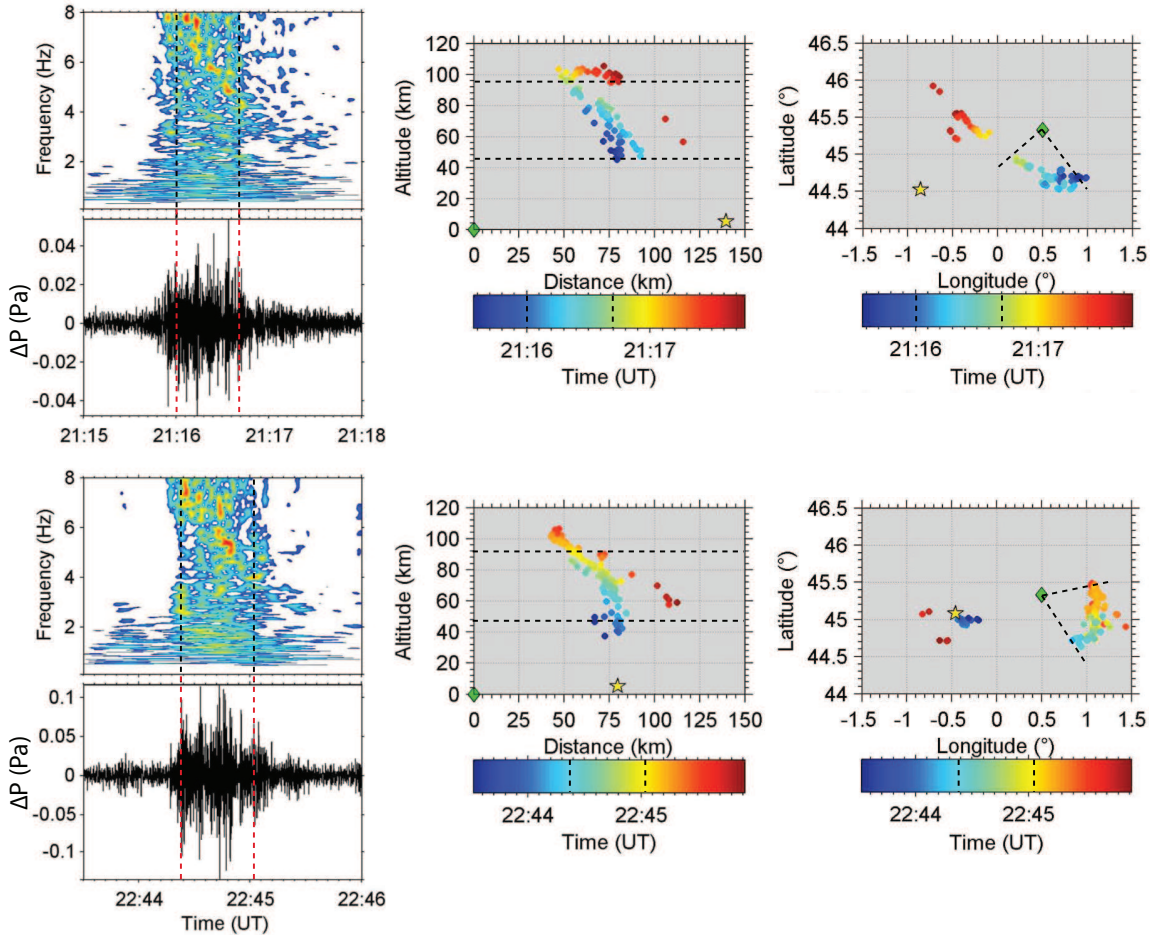

Figure 5.3. Two examples of long-duration events showing their pressure signals (0.1-9 Hz), their scalograms, their sources altitude vs. ground distance from station and their sources positions on a map. The green diamond indicates the position of the infrasound station, and the yellow star the position of the parent lightning [*Farges and Blanc*, 2010]. The dashed lines on the left panels show the time extent of the inverted chirp for each event. The dashed lines are then reported on the two right panels to show the altitude and azimuthal extent of the inverted chirp source.

observed but no infrasonic signal could be related to these events, most likely because the sprites were too small and weak. The two inverted chirp signatures presented on Figure 5.3 are attributed to sprites located about 75 km from the infrasound station. The measured signals typically have a duration of 1 min and an amplitude between 10^{-2}-10^{-1} Pa.

The analysis of total energy budget associated with sprite and causative lightning discharges indicates that the observed infrasonic signatures are most likely

produced by direct Ohmic heating of air in sprite columns due to a passage of electric current. Adopting a hypothesis that the heating is the primary mechanism, the strength of observed infrasound emissions may appear to contradict available analysis of air heating in sprite streamers giving relatively small temperature changes $\Delta T/T \sim$0.2-2% [*Pasko et al.,* 1998], an accurate analysis of energy budget of sprite discharges indicating $\Delta T \leq$ 0.5 K [*Sentman et al.,* 2003], and limited information on sprite rotational temperature indicating consistency of observed molecular nitrogen band emissions with rotational temperatures in the range 220-230 K (not exceeding 300 K) [*Green et al.,* 1996; *Morrill et al.,* 1998; *Bucsela et al.,* 2003; *Kanmae et al.,* 2007]. Preliminary estimates reported in [*Pasko and Snively,* 2007] indicate, however, that magnitudes of observed sprite infrasound signatures are consistent with weak air heating in streamer channels in sprites on the order of several degrees K.

Both the long-range and close-range observations of sprite attributed infrasonic signals are yet to be interpreted. A mechanism for the long-range chirps generation has been proposed by *Farges et al.* [2005], but has yet to be tested with propagation models. Close-range inverted chirps are a very recent observation, and no suggestions have yet been made on how they could be generated. In this chapter we will look further into these two phenomena to propose a more detailed explanation of their occurrence.

5.2 Modeling of Close Range Infrasonic Signals

Let us first look into close-range observations which we refer to as inverted chirps. Information on infrasound generation altitude depending on their arrival time can be retrieved from Figure 5.3, which suggest that the infrasound signal is strongly related to the sprite vertical extent. Remembering that the absorption scales up with altitude and depends on the square of frequency, it can be hypothesized that absorption scaling through the sprite vertical extent is at least partly responsible for the observed infrasonic signal. Specifically we expect that the signal arriving from higher altitudes would naturally have a depleted high frequency content. Also, geometrical considerations indicate that such a signal would arrive to an observer positioned several tens of kilometers horizontal distance from the sprite

with some delay with respect to the signal emitted from the lower portions of the sprite.

Additionally, observations from [*Gerken and Inan*, 2003] and streamer simulation results [e.g., *Liu and Pasko*, 2004] show that streamers radii increase with altitude. Overall trend of streamers scaling is expected to proceed inversely proportionally to ambient neutral density in the atmosphere [e.g., *Liu and Pasko*, 2004]. This alone would lead to a factor of 600 wider streamers at 90 km in comparison with streamers at 45 km. Streamers in sprites, however, accelerate, expand and branch and particular diameters realized at specific altitudes depend on geometry of applied reduced electric field and history of sprite initiation and development [*Liu et al.*, 2009]. Based on observational evidence [e.g., *Gerken and Inan*, 2003] it can be assumed for quantitative estimates that low altitude streamers in sprites would have diameters d_s of 10 to 50 m, while high altitude streamers may have diameters exceeding 200 m. Combined with speeds of sound c_s of $\sim$320 m/s and $\sim$280 m/s at $\sim$45 km and $\sim$90 km altitudes respectively [*Sutherland and Bass*, 2004], this suggests dominant infrasonic frequencies $f \simeq c_s/d_s$ of $\geq$8 Hz for the lower part of the sprite and $\leq$1 Hz for the upper part of the sprite, assuming that pressure perturbation in streamer columns (i.e., due to heating) forms on time scales $\tau_s \ll d_s/c_s$.

We can summarize our hypothesis as follows:

1. Signal from the lower altitude of the sprite arrives first (from $\sim$45 km) following a direct propagation path with very minimal absorption; low absorption results in a full conservation of the signal frequency content.

2. Signal from the upper altitude of the sprite arrives last (from $\sim$95 km) following a direct propagation path with a strong absorption; high absorption results in a low-pass filtering of the signal frequency content.

3. Fine structure of sprites at low altitudes would generate predominantly high infrasonic frequencies ($\sim$8 Hz).

4. Wider sprite structures at high altitudes would generate predominantly low infrasonic frequencies ($\sim$1 Hz).

5.2.1 Ray-tracing modeling

As it requires the investigation of infrasound with high frequencies over large domain, the study of inverted chirps generated by sprites has to be conducted very carefully; to resolve a frequency of 8 Hz, a spatial step of 3 m over domain of 150 km high by 100 km wide is needed, which would not only require a long computation, but also ∼80 GB of physical memory. In order to get initial insight we first analyze the problem with ray-tracing simulations performed with the HARPA ray-tracing program [e.g., *Jones*, 1996].

Figure 5.4 shows ray-tracing results for different source vertical and horizontal extents. In this part we will only focus on results from panel (a). For this situation we model the sprite vertical extremums by two monochromatic point sources with frequency 6 Hz. We investigate rays propagating downward that can be observed around 75 km horizontal distance from the sprite on the ground. It first appears as suggested by observations that the rays from the lower part of the sprite arrive first, followed after ∼1 min by rays from the upper part of the sprite. It can also be noticed that the signal from 45 km altitude is barely attenuated (∼0.02 dB), while the signal from 100 km altitude is much more attenuated for the same frequency (∼7 dB). Supposing that the infrasound intensity generated at the lower altitude of the sprite is of the same order of magnitude than the infrasound generated at the higher part of the sprite, this result alone would suggest that acoustic absorption is greatly responsible for the observed inverted chirp signatures.

While the ray-tracing results seem to support hypothesis 1 and 2 mentioned at the beginning of this section, quantitative results are needed to know the relative importance of the effect of the altitude dependency of absorption and of the streamers radii. A proper model of the sprite is also required to understand this phenomena.

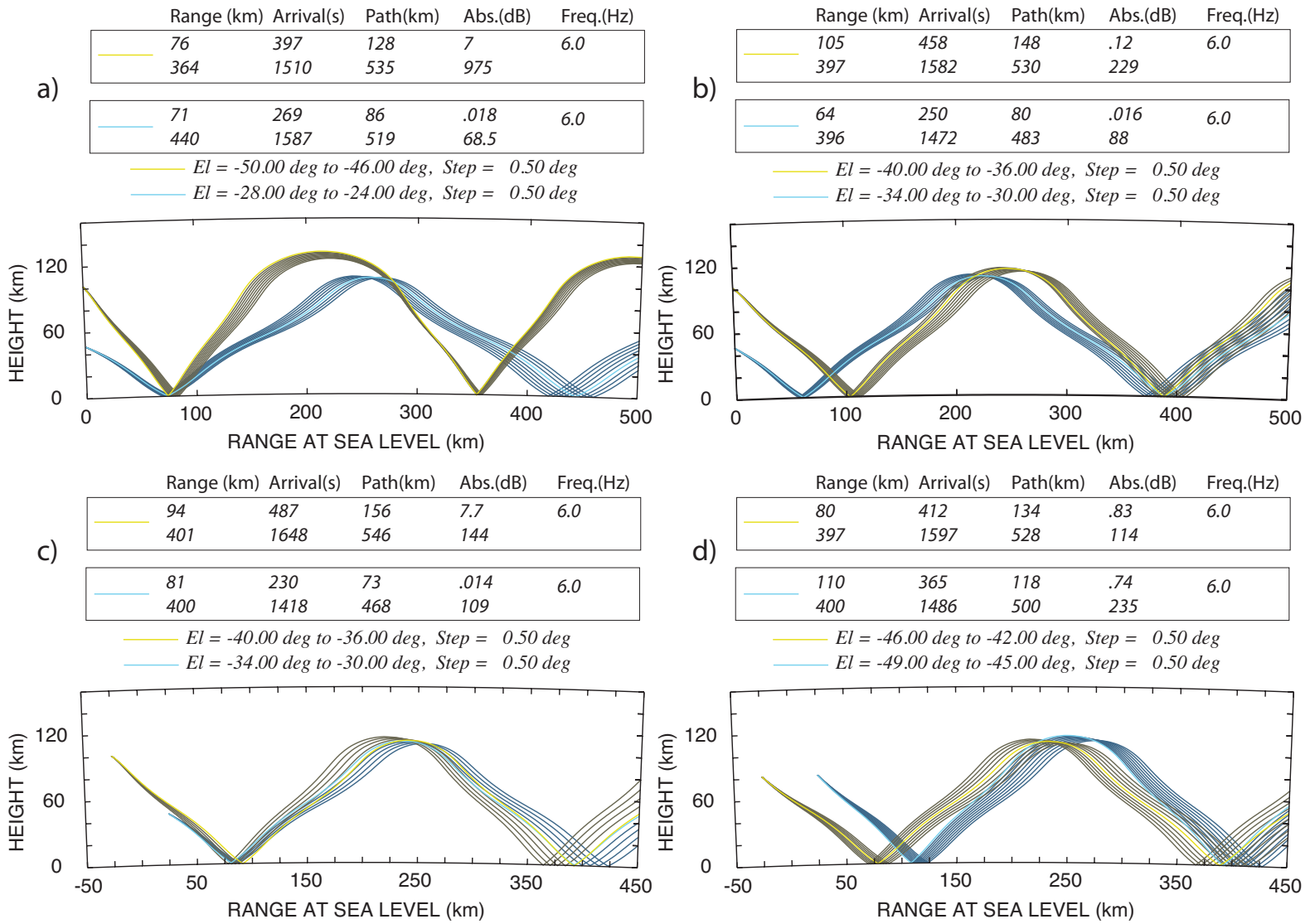

Figure 5.4. Ray-tracing results for different scenarii obtained with HARPA model. (a) Sources at 45 km and 100 km altitudes with rays intercepting at r ∼75 km. (b) Same sources as (a) intercepting at r ∼400 km. (c) Sources at 45 km and 100 km altitudes and 50 km apart horizontally. (d) Sources at 80 km altitude and 50 km apart horizontally intercepting at r ∼400 km.

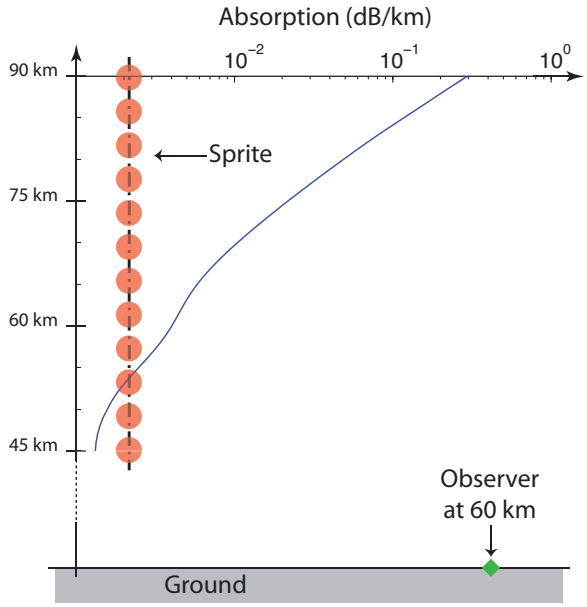

Figure 5.5. Cross sectional view of the sprite in the model domain illustrating the parameters and geometry of the domain. This figure also includes the absorption coefficient adapted from [*Sutherland and Bass*, 2004] for a 3 Hz infrasonic wave propagating between 45 km and 90 km altitude.

5.2.2 FDTD modeling

Sprites have a very complex geometry that would be difficult to reproduce numerically. However, to verify our hypothesis we can imagine a simplified geometry that would accurately reproduce infrasound generation from a sprite. Figure 5.5 describes how we represent the sprite in our numerical model: each sphere is given a specific frequency content which varies from high to low frequencies with increase altitude. The spheres are then pulsated to generate pressure waves for a given time duration corresponding to the travel time of an infrasonic wave through the width of the sprite. For instance, if a sprite is 30 km wide, the spheres will be pulsated for a total of 100 s. The vertical distribution of the spheres combined with the duration of the pulsation of each sphere effectively reproduce the expected infrasonic radiation of the sprite.

The absorption coefficient for a frequency of 3 Hz has been added to Figure 5.5 to emphasize that absorption and sprite radii are very important considerations in our investigation.

We illustrate the effect of the sprite frequency content assuming the frequency

range 0.1-0.9 Hz. The effects of absorption are not included in this part. Each one of the 15 sources composing the modeled sprite is assumed to radiate for 40 s to account for the large number of streamers within the sprite (i.e., effectively representing sprite with 12 km transverse extent assuming c_s∼300 m/s). The frequency distribution is set to vary linearly with altitude, from high to low frequencies. Figure 5.6(a) provides a 2-D snapshot of the normalized pressure perturbation $\tilde{p}/p_0(z)\sqrt{p_0(z)/p_0(z_{\text{ref}})}$ at time $t = 200$ s, where $p_0(z)$ is the ambient profile of pressure as a function of altitude z and $z_{\text{ref}} = 45$ km. The related observed pressure perturbation at 60 km horizontal distance, as well as the corresponding spectrogram of the signal are presented in Figure 5.6(b) and (c). The same simulation is repeated using a second and fourth order variation of frequency as a function of altitude such as $f = (0.1 - 0.9)(z - 45)^n/45^n + 0.9$ for 45 km $\leq z \leq$ 90 km, where z is the altitude in km and n is the order of the frequency variation. The dynamic spectrograms of the observed pressure perturbation at 60 km horizontal distance are presented in Figure 5.7(a) and (b).

The effect of the altitude scaling of absorption on the frequency content of the sprite is then illustrated. In order to accelerate computations, the present study employs a model set up with vertical and horizontal grid resolution of 50 m, allowing to accurately model frequencies $f \leq 0.5$ Hz. The absorption is artificially increased so that the maximum frequency represented (0.5 Hz) is attenuated as much as a frequency of 6 Hz would be attenuated under standard atmospheric conditions. The multiplication factor of the absorption coefficient is determined using the quadratic dependency of absorption on frequency [e.g., *Sutherland and Bass*, 2004], which yields a factor of 150. Figure 5.8 shows the results from the modeling of two sources positioned at altitudes 45 and 90 km each radiating both 0.05 Hz and 0.4 Hz equal magnitude signals.

5.2.3 Discussion

It has been mentioned previously that modeling results [*Liu and Pasko*, 2004] suggest streamer radius of a few tens of meters at 70 km altitude. Given a speed of sound of ∼290 m/s at this altitude, it is expected that frequencies up to 8 Hz would be generated. However, the absorption of an 8 Hz acoustic wave at 70 km altitude

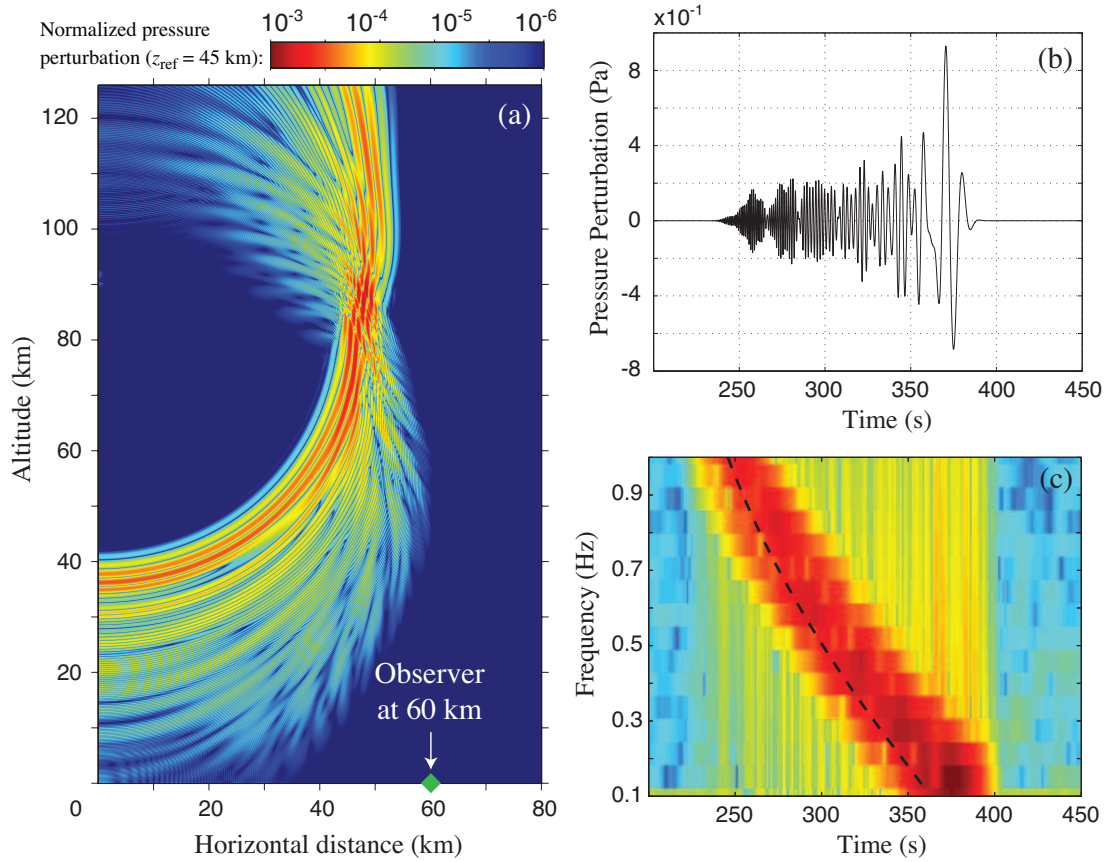

Figure 5.6. Modeling results for a sprite consisting of 15 isotropic sources radiating frequencies linearly varying from 0.1 Hz at 45 km altitude up to 0.9 Hz at 90 km altitude. (a) Snapshot of the normalized pressure perturbation at t=200 s (b) Pressure perturbation signal observed on the ground at 60 km horizontal distance. (c) Spectrogram of the observed signal (the dashed line represents the expected shape when accounting for direct propagation).

is ∼0.2 dB/km [e.g., *Sutherland and Bass*, 2004], suggesting that such a wave would be mostly absorbed before reaching the ground. Figure 5.8 evidences that the high frequencies generated at high altitudes are mostly absorbed and consequently not observed on the ground. As a result, the high frequencies generated in the upper part of the sprite are most likely to dissipate before reaching the ground. This effect, leading to arrival of only low frequencies at the end of the sprite generated waveform may contribute to the formation of inverted-chirp signals observed on the ground at close range [*Farges and Blanc* 2010].

The scaling of transverse dimension of streamers with altitude is expected to

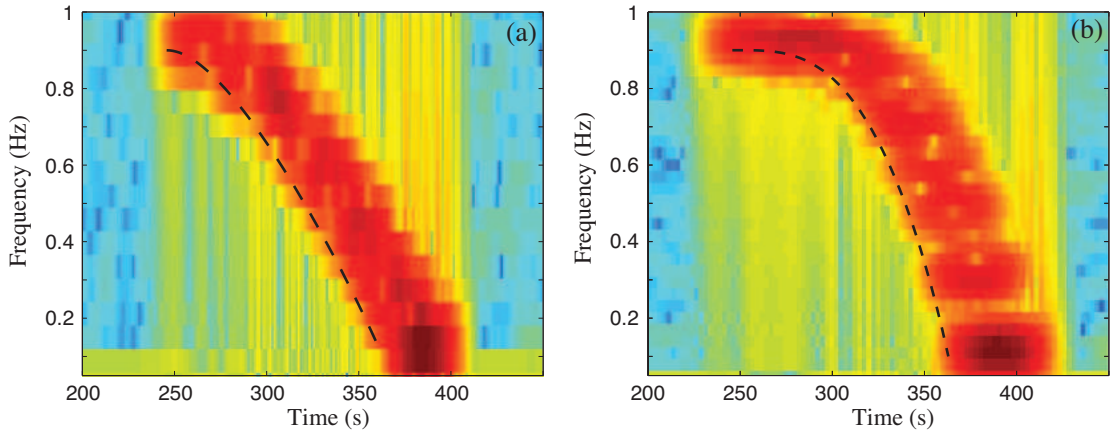

Figure 5.7. Panels (a) and (b) are the same as in Figure 5.6(c) only for sources with radiated frequencies varying as a second and fourth order function of altitude, respectively, from 0.9 Hz at 45 km to 0.1 Hz at 90 km.

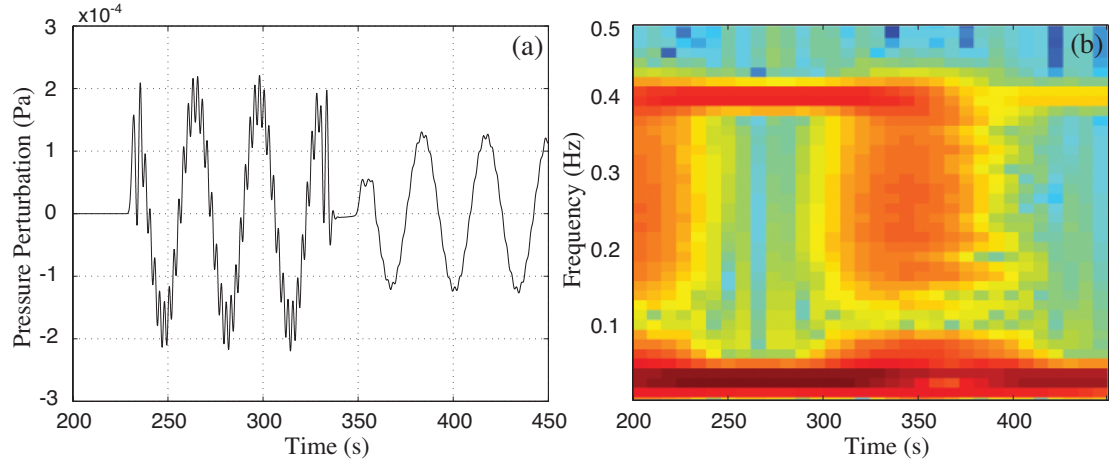

Figure 5.8. Modeling results for two isotropic sources (both radiating frequencies 0.05 Hz and 0.4 Hz) positioned at 45 km and 90 km altitudes in an atmosphere with an absorption artificially increased by a factor of 150 with respect to its standard value. (a) Pressure perturbation signal observed on the ground at 60 km horizontal distance. (b) Spectrogram of the observed signal.

be a factor responsible for the frequency content of the sprite and consequently the observed inverted chirp. Results presented in Figure 5.6(c) show a linear inverted chirp on the dynamic spectrogram effectively mapping the altitude frequency distribution in the modeled sprite. It should be noted that while the frequency content and time extent of the inverted chirp are not exactly those observed by *Farges and Blanc* [2010], the results still demonstrate the effect of the propagation

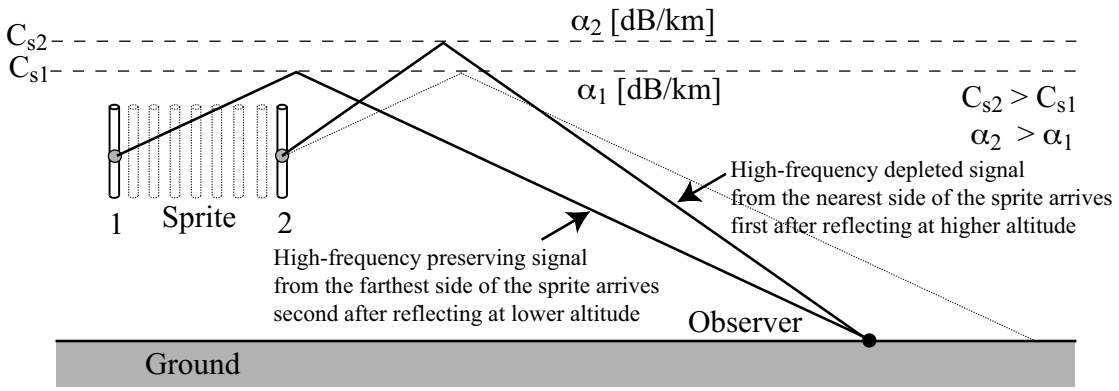

Figure 5.9. Mechanism of infrasound chirp signal [*Farges et al.*, 2005].

and observation of infrasound from a source with the same qualitative dynamics as a sprite. Specifically, the duration of the chirp signal reported in Figure 5.6(c) exceeds that reported experimentally. This can be directly attributed to smaller vertical and horizontal extensions of sprite in experimental situation as compared to the parameters used in modeling.

The shape of the inverted-chirp in Figure 5.6(c) is directly correlated with the linear frequency distribution through the sprite vertical extent. To demonstrate this relation, the modeled sprite used in Figure 5.6 is modified using two different altitude frequency distributions in which the frequency drops as a second and fourth order function of altitude. Figure 5.7 shows that the dynamic spectrum of the pressure perturbation observed on the ground again maps well the frequency distribution as a function of altitude in the modeled sprite. This result shows that infrasound observed at close range from sprites can be used to remote sense predominant physical dimensions of radiators (i.e., streamers) in sprites responsible for infrasonic emissions.

Modeling results presented in this work suggest that in specific experiments both the scaling of absorption with frequency and altitude, and the scaling of transverse dimension of filamentary structures (streamers) in sprites as a function of altitude may contribute to the observed inverted-chirp signal.

5.3 Modeling of Long Range Infrasonic Signals

The specific mechanism by which chirp-like infrasound signatures associated with sprites are produced is not known and the related processes have not been yet modeled on quantitative level. A possible explanation has been proposed by *Farges et al.* [2005] and illustrated in Figure 5.9. As already mentioned above the infrasound durations appear to correlate well with observed horizontal dimensions of sprites [*Farges et al.,* 2005]. In this case due to well known properties of infrasound propagation and absorption in atmosphere (see Chapter 2) the infrasound signal coming from the nearest side of the sprite (relatively to the observer) reflects at higher altitude, has reduced high-frequency content due to strong absorption at high altitudes, and arrives first at the observation point. The infrasound signal generated from the farthest side of the sprite reflects at lower altitude, has enhanced high-frequency content, and arrives second at the observation point. This hypothesis is supported by ray-tracing results and will be further investigated in the next subsection. However, other ray paths are generated from the sprite and need to be considered too. Furthermore, it can be noticed that sprites observed at long distances are typically large sprites each displaying a horizontal extent approximately equal to their vertical extent; for this reason, the influence of the vertical extent of the sprite on the observed signal will also have to be investigated. It can also be asked if the inverted chirp signal observed at close range propagates through the atmosphere where it is inverted and then observed again at a longer distance as non-inverted chirp signatures.

The important points related to the long range infrasonic signals needing further investigation are summarized bellow:

1. Is the inverted chirp observed at close range re-inverted and observed again at long range?

2. Is the chirp signal related to the vertical extent of the sprite?

3. Is the chirp signal related to the horizontal extent of the sprite?

4. Is the chirp signal related to the diagonal extent of the sprite?

5. What is the dominant ray-path responsible for the chirp signal?

5.3.1 Ray-tracing modeling

We know refer to Figure 5.4 again and consider ray path reaching ∼400 km horizontal distance from the sprite. Our first question can be answered using results from panel (a); it appears that the rays responsible for the inverted chirp observed at close range, after being reflected on the thermosphere are observed almost a 100 km apart, and cannot be observed by the same ground observer.

The vertical extent influence of the sprite on the long range observations is detailed in panel (b). The rays from the low part of the sprite arrive ∼100 s before the rays from the upper part of the sprite which matches observations. However the signal arriving first is much less absorbed due to a lower altitude reflection than the signal arriving last. This implies that if the vertical extent of the sprite was the main factor in the observed infrasonic signal, we would obtain an inverted chirp and not a chirp.

The diagonal extent influence of the sprite on the long range observations is detailed in panel (c). First and last signals arrive more than 200 s apart, which is longer than observed. In addition, both first and last arrival are similarly absorbed, which would result in an observed signal with very little frequency variation.

Finally the horizontal extent of the sprite on the long range observations is detailed in panel (d). Results confirm *Farges et al.* [2005] initial calculations, both for the duration of the observed signal (∼100 s) and for its likely frequency content: both rays originate at the same altitude, thus suggesting a similar initial frequency content, but the ray arriving first is reflected higher in the thermosphere and consequently experience a greater absorption of its high frequencies.

The cases presented above assume that the main ray path to be considered is the ground-thermosphere ground propagation path. This path produces one of the strongest signal for observations at horizontal distances ∼400 km from the sprite source [*Farges et al.*, 2005]. It should be noticed that there exists a variation of that ground-thermosphere-ground path that reflects higher in the thermosphere and is consequently more absorbed (see Figure 5.10). This alternative path will not, however, affect the chirp signal as it is much less intense.

The ray-tracing results also suggest that the thermosphere-ground propagation path (see Figure5.10) yields a similar absorption as the lower reflecting ground-thermosphere-ground path, thus suggesting that both paths have the same impor-

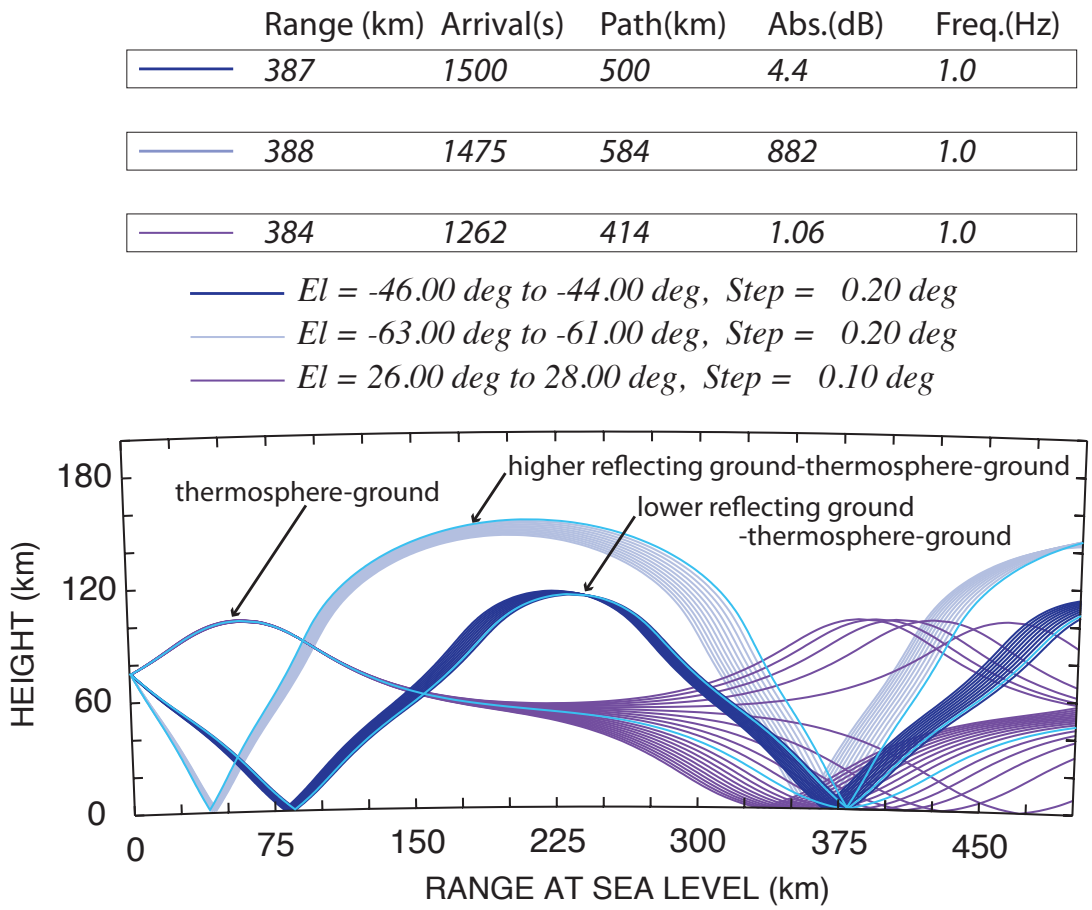

Figure 5.10. HARPA Ray-tracing results of different ground-thermosphere-ground ray paths scenario for a source at 75 km altitude with frequency 1 Hz.

tance. This reasoning suggests that a low reflecting ground-thermosphere-ground path and a thermosphere-ground path as ilustrated in Figures 5.10 can explain the observed infrasonic chirp. It should be noticed, however, that the signals generated from those two paths arrive ∼4 min apart which has not been reported in observations.

Ray tracing results allow for a more specific definition of the source geometry that should be considered for the study of infrasound from sprites observed at long distance from the source. The results can be summarized as follows:

- The chirp signal is related to the horizontal extent of the sprite.
- The dominant ray paths observed at 400 km are a ground-thermosphere-ground and a thermosphere-ground paths.

5.3.2 FDTD modeling

Using a very simple cylindrical pressure perturbation located at 75 km altitude, we are able to observe that the ground-thermosphere-ground path (marked as 4) indeed gives one of the highest amplitude of pressure perturbation in agreement with *Farges et al.* [2005]. The pressure wave is launched by uniform heating (p'/p_0=0.01) inside of a cylindrical volume with radius R=1.5 km and height H=5 km, centered at altitude z_{ref}=75 km. It can be noticed in Figure 5.11 that there are four main infrasound arrivals: the first weaker one corresponds to a high-loss thermospheric reflection, the second arrival correspond to the direct propagation path, the third arrival corresponds to a thermosphere-ground propagation, and the last intense arrival is due to a low loss ground-thermosphere-ground path as was initially proposed by *Farges et al.* [2005]. Figure 5.12 confirms that the last arrival, corresponding to the ground-thermosphere-ground propagation path is also one of the strongest. It also appears that the thermosphere-ground path (marked as 3) gives a similar amplitude of pressure perturbation and may have to be considered in the chirp generation mechanism. The high-loss thermospheric reflection (marked by 1) is very weak and can barely be observed in Figure 5.12.

Further development of our modeling will investigate the full frequency content of the sprite as designed in Section 5.2.2. This should allow for the verification of the hypothesis that the atmosphere's absorption is responsible for creating the infrasonic chirp signature observed at ∼400 km horizontal distance from the sprite.

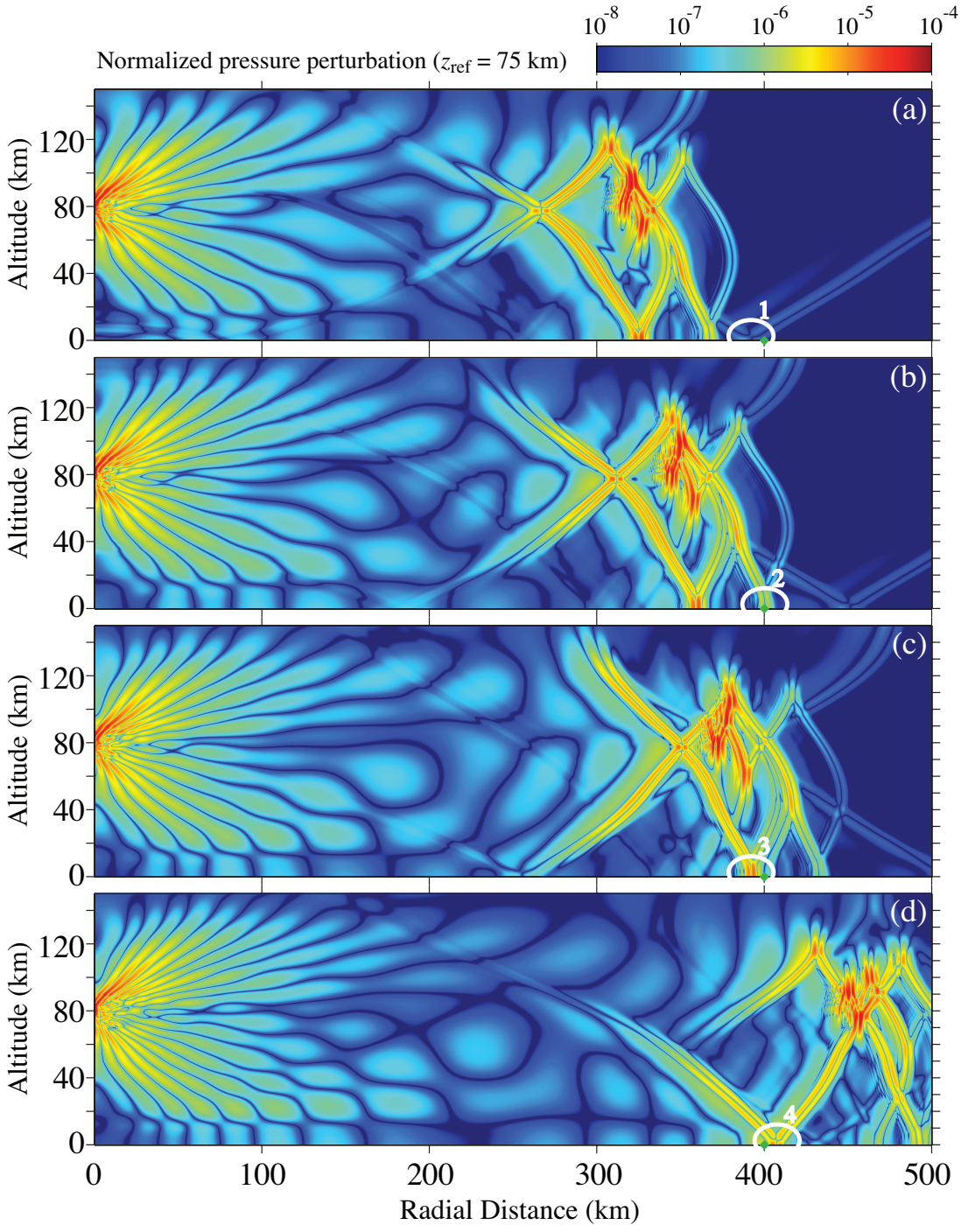

Figure 5.11. Snapshot of the normalized pressure perturbation at: (a) t=1200 s, (b) t=1300 s, (c) t=1400 s, (d) t=1700 s

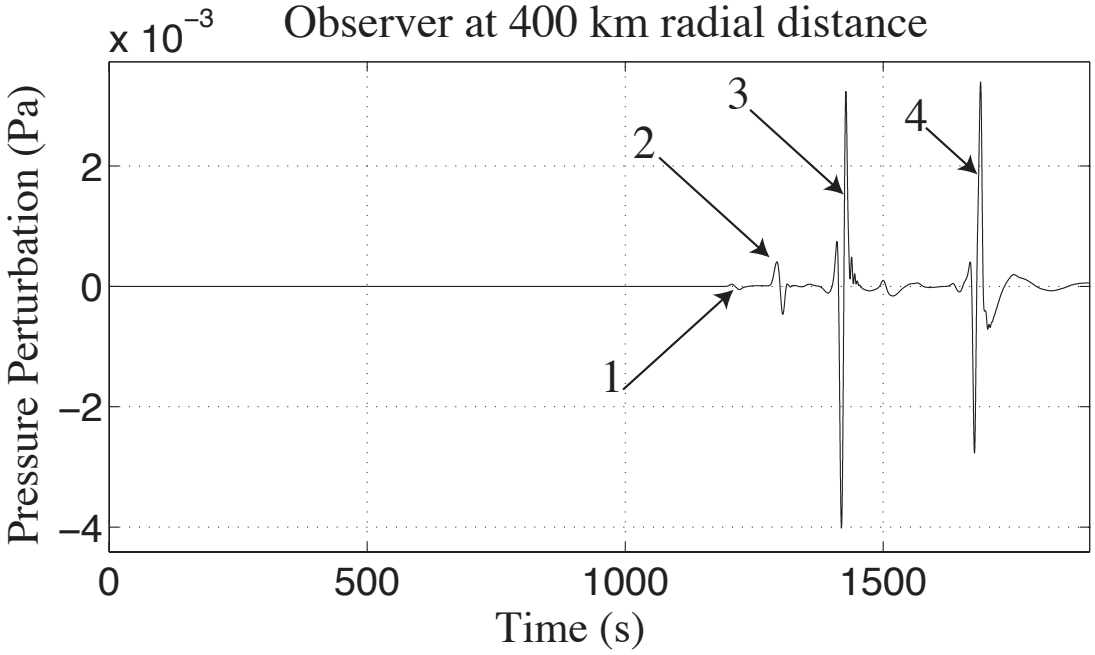

Figure 5.12. Pressure perturbation on the ground at r=400 km.

Chapter 6

Summary and Suggestions for Future Research

6.1 Summary of Results

The principal scientific contributions presented in this report can be summarized as follow:

- Development of 1-D and 2-D finite-difference time-domain (FDTD) models based on linearized equations of acoustics employing the realistic atmospheric structure and infrasound absorption algorithms advanced by *Sutherland and Bass* [2004].
- Implementation, in framework of the 1-D and 2-D FDTD models, of a decomposition technique for efficient modeling of infrasound absorption in a realistic atmosphere recently proposed by *de Groot-Hedlin* [2008].
- Parallelization of the 2-D model using a domain decomposition technique enabling faster computation and memory distribution.
- Our studies of infrasound produced by pulsating auroras confirm the validity of assumption of *Wilson et al.* [2005] concerning 1-D (planar) representation of the source of pulsating aurora. However, results also demonstrate critical importance of scaling of pressure perturbation proportionally to root square

of ambient pressure in a gravitationally stratified atmosphere for derivation of accurate magnitudes of infrasonic waveforms on the ground.

- Modeling results on infrasound from pulsating auroras indicate that fluxes on the order of 50 erg/cm^2/s are needed to explain pressure waves magnitudes of 0.05 Pa observed on the ground. This energy is unlikely to be provided exclusively by precipitating electrons, and Joule heating associated with the electrojet modulated by the pulsating aurora may be responsible for part of the deposited energy.

- Modeling results of sprite generated infrasound observed at close range (∼75 km) emphasize the importance of both the atmospheric absorption and scaling of transverse dimension of filamentary structures (streamers) in sprites as a function of altitude to explain the observed inverted chirps.

- Modeling results confirm the validity of an assumption by *Farges et al.* [2005] that the infrasound signature from sprite observed at long distance from the source is due to a ground-thermosphere-ground propagation of the infrasound radiated from the sprite.

- Preliminary results from ray-tracing analysis suggest that sprite generated infrasound observed at long distance from the source (∼400 km) are generated by a deposition of energy within a small vertical extent at a given altitude (∼70-80 km) within the horizontal extent of the sprite.

6.2 Suggestions for Future Research

Aside from designing and investigating other reported infrasound sources, the model itself could be improved by including effects such as background wind. In addition, a more local approach to specific observations could be implemented by using atmospheric measurements obtained at given location and time for more realistic representation of the background atmosphere.

The model presented in this thesis is based on a specific numerical scheme chosen for its advantages in terms of speed and accuracy. There exist many other finite difference schemes that could also easily be substituted in the existing code.

One interesting example to investigate would be the use of a Dispersion Relation Preserving (DRP) scheme: this type of scheme is computationally demanding, but presents the advantage to guarantee an accurate propagation with a resolution as low as four points per wavelength [e.g, *Millet et al.*, 2007, and references therein]. Comparison with the scheme used in the current model would be a very important validation of the results presented in this thesis.

On aurora, more data is needed on energy deposition within the aurora. The coupling between the pulsating aurora and the electrojet needs to be better understood. Once more knowledge is acquired on these points, new numerical simulations of infrasound generation from pulsating auroras can be implemented and compared with observations to validate the energy budget of the pulsating aurora.

On sprites, higher resolution modeling results are indispensable to fully validate our hypothesis. In addition, it would be very helpful to obtain both long range and close range infrasound measurements from the same group of sprites. One possible way of achieving these observations would be to place two infrasound stations separated by $\sim$500 km on typical storm paths for a long period of time. Such an experiment would allow for a very accurate description of the energy budget of sprites using numerical simulations.

Other events such as supersonic auroras [e.g., *Wilson and Nichparenko*, 1967] can be investigated using the model developed in this thesis, especially now that it has been shown how infrasound observations could be used to retrieve valuable information if properly interpreted.

Appendix A

Algorithm for absorption decomposition

This appendix summarizes the algorithm used to decompose the absorption coefficient $\alpha(z)$ as $\beta(z)+\gamma(z)f^2$ (Figure A.1). As illustrated in Figure A.2, the difficulty is that the absorption coefficient $\alpha(z)$ cannot be approximated as a quadratic function of frequency at every altitude: above a 120 km and between 10-50 km, the quadratic approximation is not optimal. However, between 10-50 km, absorption of infrasonic frequencies is so weak, that the wave would not be significantly affected by inexact absorption coefficients. Concerning altitudes above 120 km, only very low frequencies (less than 1 Hz) would survive, so that it only matters that absorption coefficients for these very low frequencies are computed properly. As can be noticed in the flow chart (Figure A.1), the algorithm strongly depends on a correct initial guess. The first approximation is made for the absorption at the maximum altitude (160 km), and each subsequent guess for each subsequent altitude is chosen to be the result of the previous altitude step. A key feature of the program is the algorithm provided by the Matlab function "lsqnonlin" to minimize the sum of squares of a function. This function was chosen empirically among other equivalent Matlab functions because it provided the best minimization of our norm (see Figure A.1).

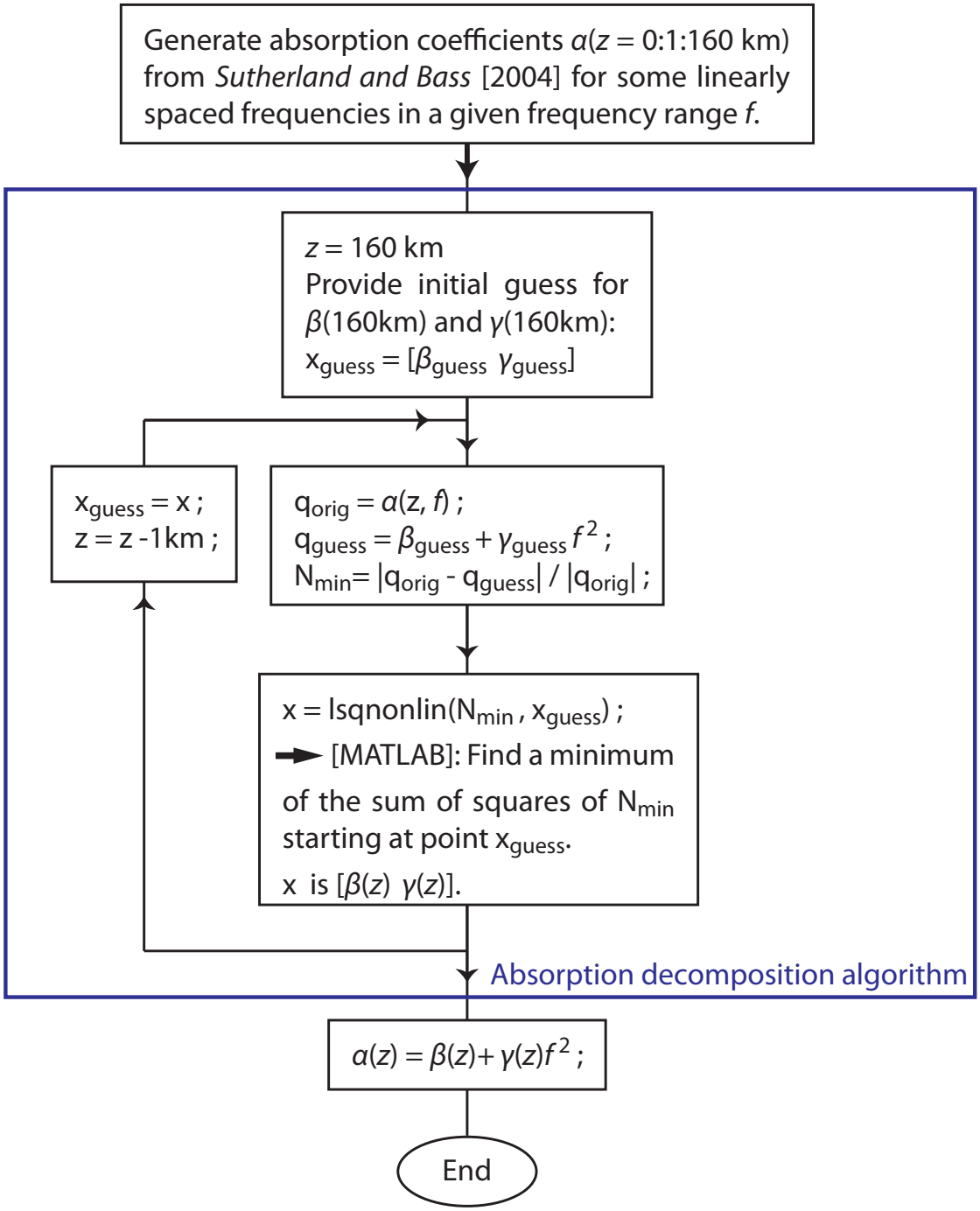

Figure A.1. Flow chart of the algorithm designed to compute decomposed absorption coefficients $\beta(z)$ and $\gamma(z)$.

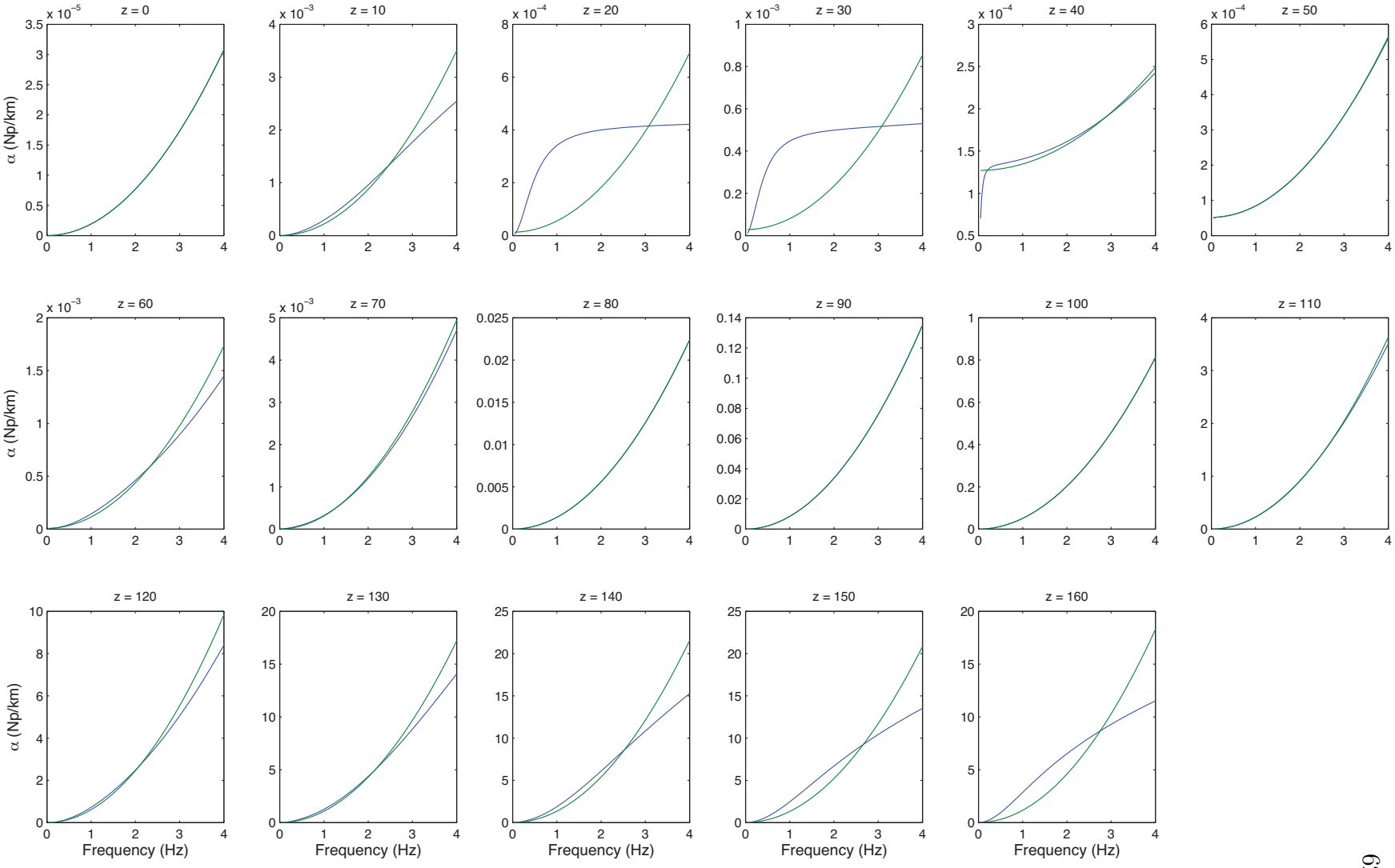

Figure A.2. Absorption coefficient (blue curves) and its associated least-square fit (green curves) plotted every 10 km over the frequency range 0.05-4 Hz.

References

Arrowsmith, S. J., D. P. Drob, M. A. H. Hedlin, and W. Edwards (2007), A joint seismic and acoustic study of the Washington State bolide: Observations and modeling, *J. Geophys. Res.*, *112*, D09304, doi:10.1029/2006JD008001.

Assink, J. D., L. G. Evers, I. Holleman, and H. Paulssen (2008), Characterization of infrasound from lightning, *Geophys. Res. Lett.*, *35*(15), L15802, doi:10.1029/2008GL034193.

Bass, H. E., L. C. Sutherland, J. Piercy, and L. Evans (1984), Absorption of sound by the atmosphere, in *Physical Acoustics*, vol. XVII, edited by W. P. Mason and R. N. Thurston, chap. 3, pp. 145–231, Academic, New York.

Bass, H. E., H. J. Bauer, and L. B. Evans (1972), Atmospheric Absorption of Sound - Analytical Expressions, *J. Acoust. Soc. Am.*, *52*(3), 821–825.

Bedard, A. J. (2005), Low-frequency atmospheric acoustic energy associated with vortices produced by thunderstorms, *Month. Weather Rev.*, *133*(1), 241–263.

Bedard, A. J., and T. M. Georges (2000), Atmospheric infrasound, *Phys. Today*, *53*(3), 32–37.

Bedard, A. J., W. A. Lyons, R. A. Armstrong, T. E. Nelson, B. Hill, and S. Gallagher (1999), A search for low-frequency atmospheric acoustic waves associated with sprites, blue jets, elves, and storm electrical activity, *Eos Trans. AGU*, *80*(46), F227, Fall Meet. Suppl., Abstract A51B-18.

Blanc, E. (1985), Observations in the upper-atmosphere of infrasonic waves from natural or artificial sources - a summary, *Annales Geophysicae*, *3*(6), 673–687.

Brown, N. B., T. N. Davis, T. J. Hallinan, and H. C. Stenbaek-Nielsen (1976), Altitude of pulstaing aurora determined by a new instrumental technique, *Geophys. Res. Lett.*, *3*(7), 403–404.

Bucsela, E., J. Morrill, M. Heavner, C. Siefring, S. Berg, D. Hampton, D. Moudry, E. Wescott, and D. Sentman (2003), $N_2(B^3\Pi_g)$ and $N_2^+(A^2\Pi_u)$ vibrational distributions observed in sprites, *J. Atmos. Solar Terr. Phys.*, *65*, 583–590.

Cummer, S. A. (2003), A simple, nearly perfectly matched layer for general electromagnetic media, *IEEE Microw. Wirel. Compon. Lett.*, *13*(3), 128–130, doi: 10.1109/LMWC.2003.810124.

Davidson, G. T., and R. D. Sears (1980), Pulstaing aurorae - evidence for flux limiting, *Geophys. Res. Lett.*, *7*(3), 185–188.

de Groot-Hedlin, C. (2008), Finite-difference time-domain synthesis of infrasound propagation through an absorbing atmosphere, *J. Acoust. Soc. Am.*, *124*(3, Part 1), 1430–1441, doi:10.1121/1.2959736.

de Larquier, S., V. P. Pasko, H. C. Stenbaek-Nielsen, J. V. Olson, and C. R. Wilson (2009), Finite-difference time-domain modeling of infrasound from pulsating auroras and comparison with recent observations, *Eos Trans. AGU*, *90(52)*, Abstract A13D–0253.

de Larquier, S., V. P. Pasko, H. C. Stenbaek-Nielsen, J. V. Olson, and C. R. Wilson (2010), Finite-difference time-domain modeling of infrasound from pulsating auroras and comparison with recent observations, *Geophys. Res. Lett.*, *37*, L06804, doi:10.1029/2009GL042124.

Dessa, J. X., J. Virieux, and S. Lambotte (2005), Infrasound modeling in a spherical heterogeneous atmosphere, *Geophys. Res. Lett.*, *32*(12), L12808, doi: 10.1029/2005GL022867.

Drob, D. P., J. M. Picone, and M. Garces (2003), Global morphology of infrasound propagation, *J. Geophys. Res.-Atmos.*, *108*(D21), 4680, doi:10.1029/ 2002JD003307.

Evans, L. B., H. E. Bass, and L. C. Sutherland (1972), Atmospheric Absorption of Sound - Theoretical Predictions, *J. Acoust. Soc. Am.*, *51*(5), 1565–1575.

Farges, T. (2009), Infrasound from lightning and sprites, in *Lightning: Principles, Instruments and Applications*, edited by H. D. B. et al., chap. 18, pp. 417–432, Springer.

Farges, T., and E. Blanc (2010), Characteristics of infrasound from lightning and sprites near thunderstorm areas, *J. Geophys. Res.*, *115*, A00E31.

Farges, T., E. Blanc, A. Le Pichon, T. Neubert, and T. H. Allin (2005), Identification of infrasound produced by sprites during the Sprite2003 campaign, *Geophys. Res. Lett.*, *32*(1), L01813.

Few, A. A. (1995), Acoustic radiations from lightning, in *Handbook of Atmospheric Electrodynamics*, vol. 2, edited by H. Volland, pp. 1–31, CRC Press, Boca Raton, Fla.

Garces, M. A., R. A. Hansen, and K. G. Lindquist (1998), Traveltimes for infrasonic waves propagating in a stratified atmosphere, *Geophys. J. Int.*, *135*(1), 255–263.

Georges, T. M. (1968), HF Doppler studies of traveling ionospheric disturbances, *J. Atmos. Terr. Phys.*, *30*, 735–746.

Georges, T. M. (1973), Infrasound from convective storms: Examining the evidence, *Rev. Geophys. Space Phys.*, *11*(3), 571–594.

Georges, T. M., and W. H. Beasley (1977), Refraction of Infrasound by Upper-Atmospheric Winds, *J. Acoust. Soc. Am.*, *61*(1), 28–34.

Gerken, E. A., and U. S. Inan (2002), A survey of streamer and diffuse glow dynamics observed in sprites using telescopic imagery, *J. Geophys. Res.*, *107*(A11), 1344.

Gerken, E. A., and U. S. Inan (2003), Observations of decameter-scale morphologies in sprites, *J. Atmos. Sol.-Terr. Phys.*, *65*(5), 567–572, doi:10.1016/S1364-6826(02)00333-4.

Gilbert, K. E., and X. Di (1993), A Fast Green-Function Method for One-Way Sound-Propagation in the Atmosphere, *J. Acoust. Soc. Am.*, *94*(4), 2343–2352.

Gossard, E. E., and W. H. Hooke (1975), *Waves in the atmosphere*, Elsevier.

Green, B. D., M. E. Fraser, W. T. Rawlins, L. Jeong, W. A. M. Blumberg, S. B. Mende, G. R. Swenson, D. L. Hampton, E. M. Wescott, and D. D. Sentman (1996), Molecular excitation in Sprites, *Geophys. Res. Lett.*, *23*, 2161–2164.

Gropp, W., E. Lusk, and A. Skjellum (1999), *Using MPI : Portable parallel programming with the Message-Passing Interface*, MIT Press.

Hallinan, T. J., H. C. Stenbaek-Nielsen, and C. S. Deehr (1985), Enhanced Aurora, *J. Geophys. Res.*, *90*(NA9), 8461–8475.

Hu, W., A. Abubakar, and T. M. Habashy (2007), Application of the nearly perfectly matched layer in acoustic wave modeling, *Geophysics*, *72*(5, Suppl. S), SM169–SM175, doi:10.1190/1.2738553.

Johnstone, A. D. (1978), Pulstaing aurora, *Nature*, *274*(5667), 119–126.

Jones, R. M. (1996), Three dimensional ray tracing in the atmosphere, in *The Upper Atmosphere*, edited by W. Dieminger, G. Hartmann, and R. Leitinger, pp. 307–327, Springer Verlag, Berlin-Heidelberg.

Jones, S. L., M. R. Lessard, P. A. Fernandes, D. Lummerzheim, J. L. Semeter, C. J. Heinselman, K. A. Lynch, R. G. Michell, P. M. Kintner, H. C. Stenbaek-Nielsen, and K. Asamura (2009), PFISR and ROPA observations of pulsating aurora, *J. Atmos. Sol.-Terr. Phys.*, *71*(6-7, Sp. Iss. SI), 708–716, doi:10.1016/j.jastp.2008.10.004.

Kanmae, T., H. C. Stenbaek-Nielsen, and M. G. McHarg (2007), Altitude resolved sprite spectra with 3 ms temporal resolution, *Geophys. Res. Lett.*, *34*, L07810.

Kosch, M. J., and E. Nielsen (1995), Coherent radar estimates of average high-latitude ionospheric Joule heating, *J. Geophys. Res.*, *100*(A7), 12,201–12,215.

Kulichkov, S. N., K. V. Avilov, O. E. Popov, A. I. Otrezov, G. A. Bush, and A. K. Baryshnikov (2004), Some results of simulation of long-range infrasonic propagation in the atmosphere, *Izv. Atmos. Ocean. Phys.*, *40*(2), 202–215.

Kulichkov, S. N., I. P. Chunchuzov, G. A. Bush, and V. G. Perepelkin (2008), Physical modeling of long-range infrasonic propagation in the atmosphere, *Izv. Atmos. Ocean. Phys.*, *44*(2), 175–186, doi:10.1134/S0001433808020059.

Le Pichon, A., E. Blanc, and D. Drob (2005a), Probing high-altitude winds using infrasound, *J. Geophys. Res.*, *110*(D20), D20104, doi:10.1029/2005JD006020.

Le Pichon, A., P. Herry, P. Mialle, J. Vergoz, N. Brachet, M. Garces, D. Drob, and L. Ceranna (2005b), Infrasound associated with 2004-2005 large Sumatra earthquakes and tsunami, *Geophys. Res. Lett.*, *32*(19), L19802, doi:10.1029/2005GL023893.

Le Pichon, A., L. Ceranna, M. Garces, D. Drob, and C. Millet (2006), On using infrasound from interacting ocean swells for global continuous measurements of winds and temperature in the stratosphere, *J. Geophys. Res.-Atmos.*, *111*(D11), D11106, doi:10.1029/2005JD006690.

Le Pichon, A., J. Vergoz, P. Herry, and L. Ceranna (2008), Analyzing the detection capability of infrasound arrays in Central Europe, *J. Geophys. Res.-Atmos.*, *113*(D12), D12115, doi:10.1029/2007JD009509.

Le Pichon, A., J. Vergoz, E. Blanc, J. Guilbert, L. Ceranna, L. G. Evers, and N. Brachet (2009), Assessing the performance of the International Monitoring System's infrasound network: Geographical coverage and temporal variabilities, *J. Geophys. Res.*, *114*, D08112, doi:10.1029/2008JD010907.

Lingevitch, J. F., M. D. Collins, D. K. Dacol, D. P. Drob, J. C. W. Rogers, and W. L. Siegmann (2002), A wide angle and high Mach number parabolic equation, *J. Acoust. Soc. Am.*, *111*(2), 729–734.

Liszka, L. (2004), On the possible infrasound generation by sprites, *J. Low Freq. Noise Vib. Act. Control*, *23*(2), 85–93.

Liszka, L., and Y. Hobara (2006), Sprite-attributed infrasonic chirps - their detection, occurrence and properties between 1994 and 2004, *J. Atmos. Sol.-Terr. Phys.*, *68*(11), 1179–1188, doi:10.1016/j.jastp.2006.02.016.

Liu, N. Y., and V. P. Pasko (2004), Effects of photoionization on propagation and branching of positive and negative streamers in sprites, *J. Geophys. Res.*, *109*(A4), A04301, doi:10.1029/2003JA010064.

Liu, N. Y., V. P. Pasko, D. H. Burkhardt, H. U. Frey, S. B. Mende, H.-T. Su, A. B. Chen, R.-R. Hsu, L.-C. Lee, H. Fukunishi, and Y. Takahashi (2006), Comparison of results from sprite streamer modeling with spectrophotometric measurements by ISUAL instrument on FORMOSAT-2 satellite, *Geophys. Res. Lett.*, *33*, L01101, doi:10.1029/2005GL024243.

Liu, N. Y., V. P. Pasko, K. Adams, H. C. Stenbaek-Nielsen, and M. G. McHarg (2009), Comparison of acceleration, expansion, and brightness of sprite streamers obtained from modeling and high-speed video observations, *J. Geophys. Res.*, *114*, A00E03, doi:10.1029/2008JA013720.

Lu, G., D. N. Baker, R. L. McPherron, C. J. Farrugia, D. Lummerzheim, J. M. Ruohoniemi, F. J. Rich, D. S. Evans, R. P. Lepping, M. Brittnacher, X. Li, R. Greenwald, G. Sofko, J. Villain, M. Lester, J. Thayer, T. Moretto, D. Milling, O. Troshichev, A. Zaitzev, V. Odintzov, G. Makarov, and K. Hayashi (1998), Global energy deposition during the january 1997 magnetic cloud event, *J. Geophys. Res-Space Phys.*, *103*(A6), 11,685–11,694.

Maeda, K., and T. Watanabe (1964), Pulsating aurorae and infrasonic waves in the polar atmosphere, *J. Atmos. Sci.*, *21*(1), 15–29.

Matoza, R. S., M. A. H. Hedlin, and M. A. Garces (2007), An infrasound array study of Mount St. Helens, *J. Volcanol. Geotherm. Res.*, *160*(3-4), 249–262, doi:10.1016/j.jvolgeores.2006.10.006.

Millet, C., J. C. Robinet, and C. Roblin (2007), On using computational aeroacoustics for long-range propagation of infrasounds in realistic atmospheres, *Geophys. Res. Lett.*, *34*(14), L14814, doi:10.1029/2007GL029449.

Morrill, J. S., E. J. Bucsela, V. P. Pasko, S. L. Berg, W. M. Benesch, E. M. Wescott, and M. J. Heavner (1998), Time resolved N_2 triplet state vibrational populations and emissions associated with red sprites, *J. Atmosph. Solar Terr. Phys.*, *60*, 811–829.

Pacheco, P. (1996), *Parallel Programming with MPI*, Morgan Kaufmann.

Pasko, V. P. (2007), Red sprite discharges in the atmosphere at high altitude: the molecular physics and the similarity with laboratory discharges, *Plasma Sources Sci. Technol.*, *16*, S13–S29, doi:10.1088/0963-0252/16/1/S02.

Pasko, V. P. (2009), Mechanism of lightning-associated infrasonic pulses from thunderclouds, *J. Geophys. Res.*, *114*, D08205, doi:10.1029/2008JD011145.

Pasko, V. P., and H. C. Stenbaek-Nielsen (2002), Diffuse and streamer regions of sprites, *Geophys. Res. Lett.*, *29*(10), 1440, doi:10.1029/2001GL014241.

Pasko, V. P., U. S. Inan, and T. F. Bell (1998), Spatial structure of sprites, *Geophys. Res. Lett.*, *25*, 2123–2126.

Potter, D. (1973), *Computational Physics*, Wiley.

Royrvik, O., and T. N. Davis (1977), Pulsating aurora - local and global morphology, *J. Geophys. Res.*, *82*(29), 4720–4740.

Schecter, D. A., M. E. Nicholls, J. Persing, A. J. Bedard, Jr., and R. A. Pielke, Sr. (2008), Infrasound emitted by tornado-like vortices: Basic theory and a numerical comparison to the acoustic radiation of a single-cell thunderstorm, *J. Atmos. Sci.*, *65*(3), 685–713, doi:10.1175/2007JAS2384.1.

Sears, R. D., and R. R. Vondrak (1981), Optical-emissions and ionization profiles during an intense pulsating aurora, *J. Geophys. Res.*, *86*(NA8), 6853–6858.

Sentman, D. D., E. M. Wescott, R. H. Picard, J. R. Winick, H. C. Stenbaek-Nielsen, E. M. Dewan, D. R. Moudry, F. T. S. ao Sabbas, M. J. Heavner, and J. Morrill (2003), Simultaneous observations of mesospheric gravity waves and sprites generated by a midwestern thunderstorm, *J. Atmos. Solar Terr. Phys.*, *65*, 537–550.

Snively, J. B., and V. P. Pasko (2007), Effects of dynamic atmospheric structure on ducted gravity wave propagation, *2007 CEDAR Workshop*, Poster Session Booklet, p. 15, Santa Fe, New Mexico, June 26, 2007.

Sparrow, V. W., and R. Raspet (1991), A numerical-method for general finite-amplitude wave-propagation in 2 dimensions and its application to spark pulses, *J. Acoust. Soc. Am.*, *90*(5), 2683–2691.

Stenbaek-Nielsen, H. C., and T. J. Hallinan (1979), Pulsating auroras - evidence for noncollisional thermalization of precipitating electrons, *J. Geophys. Res.*, *84*(NA7), 3257–3271.

Sutherland, L. C., and H. E. Bass (2004), Atmospheric absorption in the atmosphere up to 160 km, *J. Acoust. Soc. Am.*, *115*(3), 1012–1032, doi:10.1121/1.1631937.

Taflove, A., and S. C. Hagness (2000), *Computational electrodynamics: the finite-difference time-domain method*, Artech House, second ed., Artech House, Boston, MA.

Weimer, D. R. (2005), Improved ionospheric electrodynamic models and application to calculating Joule heating rates, *J. Geophys. Res.*, *110*(A5), A05306, doi:10.1029/2004JA010884.

Whipple, F. J. W. (1926), Audibility of explosions and the constitution of the upper atmosphere, *Nature*, *118*, 309–313.

Whitaker, R. W., and J. P. Mutschlecner (2008), A comparison of infrasound signals refracted from stratospheric and thermospheric altitudes, *J. Geophys. Res.*, *113*(D8), D08117, doi:10.1029/2007JD008852.

Wilson, C. R. (1967), Infrasonic pressure waves from the Aurora: a shock wave model, *Nature*, *216*, 131–133.

Wilson, C. R., and S. Nichparenko (1967), Infrasonic waves and auroral activity, *Nature*, *214*, 1299–1302.

Wilson, C. R., and J. V. Olson (2005), Frequency domain coherence between high-trace velocity infrasonic signals at i53us and video data from pulsating aurora, *Inframatics*, *9*, 27–30.

Wilson, C. R., J. V. Olson, and H. C. Stenbaek-Nielsen (2005), High trace-velocity infrasound from pulsating auroras at Fairbanks, Alaska, *Geophys. Res. Lett.*, *32*(14), L14810, doi:10.1029/2005GL023188.

Wilson, C. T. R. (1920), Investigations on lightning discharges and on the electric field of thunderstorms, *Philos. Trans. R. Soc. London Sr. A*, *221*, 73–115.